

## Potential of DEM for investigation of non-consolidated flow of cohesive and elongated biomass particles

Pachón-Morales, John; Perré, Patrick; Casalinho, Joel; Do, Huy; Schott, Dingena; Puel, François; Colin, Julien

**DOI**

[10.1016/j.apr.2020.01.023](https://doi.org/10.1016/j.apr.2020.01.023)

**Publication date**

2020

**Document Version**

Accepted author manuscript

**Published in**

Advanced Powder Technology

**Citation (APA)**

Pachón-Morales, J., Perré, P., Casalinho, J., Do, H., Schott, D., Puel, F., & Colin, J. (2020). Potential of DEM for investigation of non-consolidated flow of cohesive and elongated biomass particles. *Advanced Powder Technology*, 31(4), 1500-1515. <https://doi.org/10.1016/j.apr.2020.01.023>

**Important note**

To cite this publication, please use the final published version (if applicable).  
Please check the document version above.

**Copyright**

Other than for strictly personal use, it is not permitted to download, forward or distribute the text or part of it, without the consent of the author(s) and/or copyright holder(s), unless the work is under an open content license such as Creative Commons.

**Takedown policy**

Please contact us and provide details if you believe this document breaches copyrights.  
We will remove access to the work immediately and investigate your claim.

# Potential of DEM for investigation of non-consolidated flow of cohesive and elongated biomass particles

John Pachón-Morales <sup>a1</sup>, Patrick Perré <sup>a,c</sup>, Joel Casalinho <sup>a</sup>, Huy Do <sup>b</sup>, Dingena Schott <sup>b</sup>, François Puel <sup>a</sup>, Julien Colin <sup>a,c</sup>

<sup>a</sup>LGPM, CentraleSupélec, Université Paris-Saclay, 3 rue Joliot-Curie, 91192 Gif-sur-Yvette, France

<sup>b</sup>Section Transport Engineering and Logistics, Department Maritime & Transport Technology, Faculty of Mechanical, Maritime and Materials Engineering, Delft University of Technology, Mekelweg 2, 2628CD Delft, The Netherlands

<sup>c</sup>LGPM, CentraleSupélec, Université Paris-Saclay, SFR Condorcet FR CNRS 3417, Centre Européen de Biotechnologie et de Bioéconomie (CEBB), 3 rue des Rouges Terres, 51110 Pomacle, France

## ABSTRACT

The evaluation of the flow properties of biomass powders is essential for the design of handling systems within a thermochemical valorization context. The Discrete Element Method (DEM) is a valuable tool for simulating the bulk behavior of granular materials that has rarely been used for biomass feedstocks. This work focuses on the numerical investigation of the flow of raw and torrefied biomass particles in a loose and dynamic conditioning using a rotating drum. The relevance of DEM parameters calibrated using bulk experiments (angle-of-repose, bulk density, retainment ratio) is tested by comparison with experimental data obtained using a rotating drum system. The calibrated DEM material model considers the elongated, submillimetric and cohesive nature of the biomass powder. Several flowability descriptors (Upper Angle of Stability, size of avalanches, fraction of revolution to trigger events and irregularity of the free surface) are evaluated using both experimental data and DEM simulations. DEM results reproduced well the experimental trends and distinguished between the different cohesive extent of the samples. DEM is therefore a relevant technique for assessing flowability of biomass powders in a non-consolidated dynamic flow. This paves the way for investigating the effects of particle characteristics on bulk flow, which are briefly discussed.

## Keywords

Woody biomass powder; DEM parameter calibration; Flowability; Avalanching; Multisphere approach; Coarse-graining; Particle shape; Rotating drum

## 1. INTRODUCTION

Interest in lignocellulosic biomass has sharply increased recently due to its potential as a renewable energy source to produce chemicals and gaseous or liquid biofuels. In biomass gasification processes for 2<sup>nd</sup> generation biofuel production, the granular flowability of the biomass feedstock influences the continuous, stable and controllable operation of the gasifier, which affects the design of reactors and composition of

---

<sup>1</sup> Corresponding author:

E-mail addresses : (J. Pachón-Morales) john.pachon@centralesupelec.fr, (J. Colin) julien.colin@centralesupelec.fr

38 the product gas [1–3]. Flow fluctuations, bridging and blockage of biomass particles in feeding systems of  
39 gasifiers are common industrial problems that hinder the cost-effective industrialization of biomass  
40 valorization facilities.

41 Before being fed into the gasifier, the biomass can be pre-treated, namely by torrefaction. Torrefaction  
42 is a mild pyrolysis at temperatures ranging between 200 °C and 300 °C in an inert environment. Details on  
43 the effects of torrefaction on biomass properties and its interest as pretreatment step for biomass  
44 valorization can be found in [4,5]. In addition to improving the energy density and grindability of the  
45 material, torrefaction also influences the size and shape of the particles obtained after grinding [6,7] which  
46 has an impact on flow properties.

47 Flow issues can be correctly addressed through knowledge of the flow behavior of bulk solids. Despite  
48 the relatively frequent occurrence of flow problems, little is known about the flow properties of biomass  
49 materials, which may differ significantly from those of conventional granular materials used in industry [8].  
50 So far, research on the flow properties of milled biomass has primarily focused on measurements using  
51 shear testers [6,9–13] in which powders are in a consolidated and quasi-static state.

52 Rotating drums are widely used devices for characterizing flowability of powders in a loose and dynamic  
53 state. They stand as a very practical geometry to study the flow of granular materials through, for instance,  
54 the evaluation of their avalanching behavior. The test does not require an extensive sample preconditioning,  
55 is performed quickly and can be repeated many times without operator intervention. In addition, rotating  
56 drums can detect changes in powder flowability brought by powder additives with greater precision and  
57 reproducibility than other commonly used loose-state tests such as angle-of-repose tests and bulk density  
58 measurements [14]. Although an overwhelming majority of work using rotating drums has focused on  
59 cohesionless materials [15–18], recent research [18–23] has highlighted the pertinence of the study of  
60 avalanches to assess flowability of cohesive materials such as moist pharmaceutical [24] and cocoa [25]  
61 powders. The avalanche characterization of biomass powder -which has a recognized cohesive character-  
62 could provide a new insight on the dynamic free-surface flow behavior of this material. For instance, values  
63 of the upper angle of stability obtained from rotating drum experiments have been correlated to the  
64 discharge rates at the outlet of screw feeders for biomass [12].

65 With the rapid development of high-performance computing technology, the Discrete Element Method  
66 (DEM) [26] is becoming a powerful simulation tool to understand granular dynamics, particularly in rotating  
67 drum flows [27]. Experimental evaluation of the isolated effects of shape, size or surface interactions on the  
68 flow behavior of bulk solids can be difficult to achieve since these properties are often correlated. Access  
69 to the individual particle dynamics of fine materials is also a major difficulty in experimental work. The  
70 ability to run a large number of simulations with full control of the physical properties of the system under  
71 study makes DEM simulations a cost-effective way to help overcome experimental limitations. It also gives  
72 an insight on the particle-scale phenomena taking place during flow.

73 Two approaches are commonly used in literature to study the flow of granular materials in rotating  
74 drums using DEM. First, a large number of investigations focuses on the microdynamics of particles flow  
75 within the drum, namely through the assessment of coordination numbers, collision frequencies of  
76 individual particles and velocity profiles [28–32]. A second approach includes the evaluation of global bulk  
77 characteristics such as dynamic angles of repose or the study of mixing and segregation of polydisperse  
78 populations [27,30,32–40]. The latter approach was used in this work, since flowability was assessed using  
79 bulk flow descriptors based on the motion of the mass center of the powder bed.

80 Due to limited computing power, implementation of DEM has limitations for simulating full-scale  
81 industrial applications, where large quantities of particles are involved [41]. Non-spherical particle shapes as  
82 well as cohesive behavior are also expensive features to model in DEM, mainly due to the need for more

83 complex contact detection algorithms and force models. In consequence, so far, most numerical studies on  
84 granular flow in rotating drums are restricted to either spherical, non-cohesive or coarse ( $d_p > 1$  cm)  
85 materials. However, challenging aspects of modelling biomass particles are precisely the inclusion of a  
86 realistic shape model, along with a cohesive behavior for low-particle-density and submillimetric particles.

87 The effects of particle shape on the flow behavior of non-cohesive granular materials inside rotating  
88 drum setups, using both DEM and experimental approaches, have been the subject of recent research  
89 [32,34–37,39,40,42–45]. For instance, Norouzi et al. [34] numerically studied the flow behavior of both  
90 spherical and non-spherical cohesionless polystyrene particles. They found that, at the same operating  
91 conditions (namely, rotational speed and filling ratio), the dynamic angle of repose –defined as the angle  
92 between the flat surface of particles and the horizontal axis– was greater for non-spherical than for spherical  
93 particles. Similar conclusions were drawn by Santos et al. [32] for rice grains compared to spherical glass  
94 beads. Mead et al. [36] comprehensively studied the influence of the aspect ratio, angularity, particle size  
95 distribution and inter-particle contact friction on the angle of repose obtained using a rotating cylinder in  
96 an avalanching regime. Wachs et al. [42] and Höhner et al. [39] have conducted DEM simulations of spheres  
97 and three different polyhedral particles in a rotating drum. They have found that the dynamic angle of repose  
98 increased with decreasing particle sphericity. Additionally, angular particles led to a less flat free surface of  
99 the particle bed and an intermittent flow behavior.

100 Unlike non-cohesive free-flowing materials, cohesive flow in rotating drums has been investigated far  
101 less. Granular cohesive systems may exhibit very different flow patterns and physical behavior (e. g.  
102 avalanching) than systems where cohesion is not significant [20,46]. Prior studies on DEM simulation of  
103 cohesive bulk materials in rotating drums include the study of velocity profiles [47], avalanching and surface  
104 angles [20,38,47], segregation and axial dispersion [46,48]. Brewster et al. [47] have reported that the  
105 magnitude of interparticle cohesion has a significant effect on the shape of the powder free surface. At low  
106 rotation rates and high enough interparticle cohesion, the powder free surface is convex. Decreasing the  
107 cohesion or increasing the rotation rate causes the free surface to flatten. Using DEM simulations Faqih et  
108 al. [49] have shown that the cohesion of the material is directly proportional to the standard deviation of  
109 the center of mass of a powder inside a rotating drum.

110 To obtain results that accurately reproduce experimental behavior, DEM parameters must be carefully  
111 chosen, measured or adjusted through calibration. Prior studies have used results from rotating drum  
112 experiments, predominantly the dynamic angle of repose, for DEM calibration of non-cohesive materials  
113 [32,50,51]. However, reaching a steady state may need several rotations of the drum, which requires long  
114 computation times, especially for a large number of submillimetric particles. Since calibration procedures  
115 generally involve running several batches of simulations with combined DEM parameters, the entire process  
116 would result in impractical timeframes. A first attempt for accelerating DEM calibration using rotating drum  
117 results was made by Hu et al. [27], by using the critical upper and lower angles of the first avalanche. This  
118 approach has yielded satisfactory results for spherical and non-cohesive materials. However, in the case of  
119 elongated and cohesive powders, the highly chaotic and history-dependent nature of the avalanches requires  
120 an assessment of dynamics over a long period of time.

121 As previously commented, in addition to the calibration of DEM parameters, the large number of  
122 particles of typical industrial processes is another factor that limits the use of DEM in industry [52]. Scaling  
123 up particle size is one technique that allows simulations to be run in a reasonable period. Coetzee [40] studied  
124 the effect of using upscaled particles on the dynamic angle of repose of corn grains in a rotating drum and  
125 identified a single set of calibrated parameters for all particles with scaling factors ranging from 1.0 to 4.0.  
126 Several particle scaling approaches have been proposed in literature, including exact scaling [41,53], coarse  
127 graining [54,55] and cutting-off approach [56]. A coarse-graining approach reduces computational effort by  
128 replacing individual (real) particles by representative upscaled ‘meso’-particles [55,57,58]. This approach has  
129 shown promising results for simulation of submillimetric biomass particles [59].

130 This paper presents a numerical study on the macroscopic flow behavior of raw and torrefied biomass  
131 powders in a rotating drum setup using DEM. Comparison with experimental data makes it possible to  
132 assess the relevance of DEM parameters calibration from bulk experiments, applied to a rotating drum  
133 system. Several avenues of novelty are covered in this work. First, the application of DEM and its calibration  
134 for modeling flow of a cohesive, non-spherical material that has been very rarely treated in the literature so  
135 far. Secondly, this work illustrates the use of a calibration procedure using simple and fast-to-obtain results  
136 to realistically represent biomass flow in a rotating geometry. By using raw and torrefied powders with  
137 different particle characteristics (size, shape and cohesiveness) we evaluated the ability of the calibration  
138 parameters to express different flow behaviors and set a flowability classification.

139 The results are intended to be useful in understanding the effect of particle size, shape and interparticle  
140 forces on the flowability of biomass powders in a non-consolidated and dynamic regime.

141 First, the material characteristics and the experimental setup are presented in the materials and method  
142 section. Thereafter, the DEM simulation methodology is detailed. Several relevant flowability descriptors  
143 such as the Upper Angle of Stability, the avalanche size, the fraction of revolution to trigger events and the  
144 irregularity of the free surface are evaluated from experimental data and DEM simulations. A comparison  
145 is made and comments on the effects of particle characteristics on flow behavior are finally provided.

## 146 2. Granular materials and experimental setup

### 147 2.1. Granular material preparation

148 Poplar (*Populus euro-americana* 'Koster') was used in this study as representative of a fast-growing  
149 lignocellulosic crop. A poplar tree was cut into boards that were then dried. Samples of 60×80×15 mm<sup>3</sup>  
150 were cut from a selected board.

151 The coupled effect of torrefaction and sieving on particle characteristics was considered in this work.  
152 Torrefaction was made in a batch furnace especially developed to assure homogeneous inter-particle  
153 treatment [60]. A controlled inert atmosphere, swept by a nitrogen flow, guaranteed an oxygen level below  
154 1.5%. Two treatments were performed at 240 °C and 280 °C for 1 hour according to the following protocol:  
155 (i) heating from room temperature to 100 °C at a rate of 10 °C·min<sup>-1</sup> (ii) plateau at 100 °C for 12 hours to  
156 remove bound residual water (iii) heating at a rate of 10 °C·min<sup>-1</sup> to the treatment temperature (iv) plateau  
157 at the treatment temperature for 1 hour and (v) cooling ensured by thermal losses and increased nitrogen  
158 flow into the reactor.

159 The oven-dried mass of the samples before ( $m_0$ ) and after ( $m_t$ ) torrefaction was measured to calculate  
160 the mass loss ( $ML$ ) due to heat treatment:

$$161 \quad ML (\%) = \frac{m_0 - m_t}{m_0} \cdot 100 \quad (1)$$

162 The mass loss is known to be a good indicator of the torrefaction intensity and has been successfully  
163 correlated to several properties of the treated biomass such as dimensional changes [61], energy properties  
164 [62], and flowability [6,63]. Mass losses of  $9.6 \pm 0.8$  % and  $24.5 \pm 3$  % were obtained for the samples  
165 torrefied at 240 °C and 280 °C, respectively.

166 The biomass samples (raw and treated) were ground using a *Retsch SM300* knife mill with a 1-mm  
167 trapezoidal hole bottom sieve at the outlet. Although an outlet sieve was used during grinding, the powders  
168 obtained were still quite polydisperse and had many fine particles. The timestep for DEM simulations of  
169 strongly polydispersed systems should be reduced according to the smallest particle present, which, in the  
170 case of biomass samples, would lead to impractical simulation times [64]. Therefore, the powders obtained  
after grinding were sieved to reduce polydispersity in particle size and shape. A *Retsch AS 200* vibratory sieve

171 shaker at an amplitude of 60% (1.8 mm) for 20 minutes was used along with sieves of opening 500  $\mu\text{m}$  and  
 172 710  $\mu\text{m}$ . Particle size and shape distributions were obtained using a *Sympatec-QICPIC* morphological particle  
 173 size analyzer [65]. The main descriptors of the distributions are listed in Table 1.

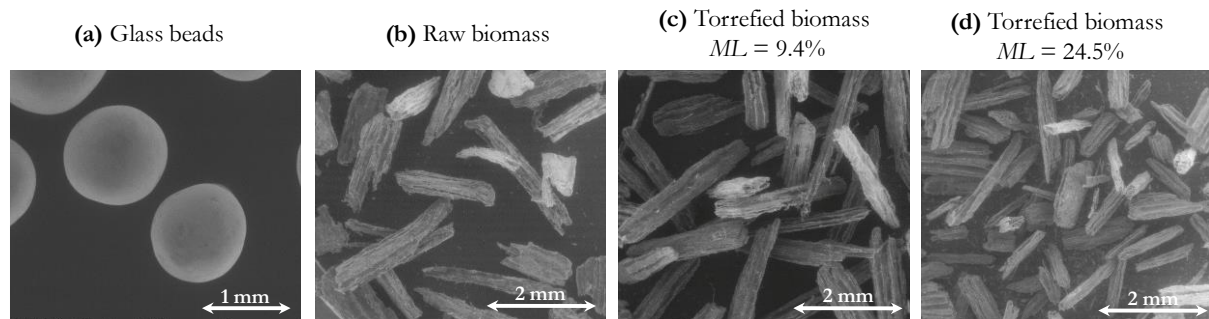
174 For comparative purposes, 1-mm diameter glass beads were used as representative of materials with  
 175 spherical and non-cohesive particles. The SEM images presented in Figure 1 depict the elongated shape of  
 176 biomass particles compared to glass beads. It is noteworthy that, despite the sieving stage, the average  
 177 particle size (minimum Feret diameter) decreased with the intensity of torrefaction. The aspect ratio values  
 178 reveal that intensively torrefied samples were also less elongated than the raw and the mildly torrefied ones,  
 179 which is likely to influence their flow properties as discussed in [66].

180 *Table 1. Sample size and shape characteristics.*

Sample	Torrefaction temperature	ML (%)	Sieving cut ( $\mu\text{m}$ )	$d_{50}^*$ ( $\mu\text{m}$ )	$d_{90}$ ( $\mu\text{m}$ )	$d_{10}$ ( $\mu\text{m}$ )	$S_d$	$a_{50}$
Glass beads	---	---	---	1212	1373	1051	0.13	0.99
Raw biomass	Untreated	0	500-710	746	1092	519	0.36	0.38
Mildly torrefied biomass	240 °C	9.6	500-710	667	929	448	0.35	0.31
Intensively torrefied biomass	280 °C	24.5	500-710	526	862	303	0.48	0.41

181 \*( $d_{50}$ ,  $d_{90}$ ,  $d_{10}$ : 50th, 90th and 10th centiles of the cumulative volume PSD, respectively,  $S_d$ : distributions span= $(d_{90}-d_{10})/(d_{90}+d_{10})$ ,  $a_{50}$ : 50th centile of  
 182 the aspect ratio distributions ( $a$ =minimum Feret diameter/maximum Feret diameter))

183



184  
 185 *Figure 1. Typical SEM images of the granular materials used in this work.*

## 186 2.2. Rotating drum and avalanching tests

187 An in-house-designed device was used to evaluate the dynamic flow behavior of the granular materials  
 188 (Figure 2). When studying avalanching behavior in rotating drums, it is crucial to ensure the absence of  
 189 external perturbations that would perturb the regular motion of powders or alter their dynamic stability.  
 190 Such a problem has already been encountered in previous research [67]. Keeping this constraint in mind, an  
 191 in-house experimental device was developed to characterize the dynamics of avalanches over a relatively  
 192 wide range of rotational speeds. Our device was designed to fulfill several constraints:

- 193 - Smooth and regular rotation avoiding any perturbation of the intrinsic powder behavior,
- 194 - Quality of lightning allowing a high shutter speed and a rigorous and easy post-processing of images,
- 195 - Drainage of electrical charges to reduce electrostatic forces effects,
- 196 - Suitable range of rotational speeds

197 The core piece of this device a stainless-steel cylinder (10 cm inner diameter, 2 cm width, roughness  $R_a$   
 198  $\approx 0.4 \mu\text{m}$ ) clamped inside a roller bearing (*IKO NAG 4924UU*) as shown in Figure 2a-b. This design is the

199 key-feature of our in-house device: it ensures a regular and smooth rotation, without vibrations and permits  
200 the uniform lighting required to grab high quality images. Two transparent conductive ITO (Indium-Tin  
201 oxide)-coated glass discs are used to ensure the drainage of static electricity. The drive mechanism, built  
202 between a motor (*maxon RE040G/PM52*) and the cylinder housing, deserves also attention. The  
203 transmission is made through two pulleys (one changeable) connected by a toothed belt. This configuration  
204 ensures a steady and stable rotational speed that can range between 0.01 rpm and 73 rpm for the chosen  
205 pulley-belt set.

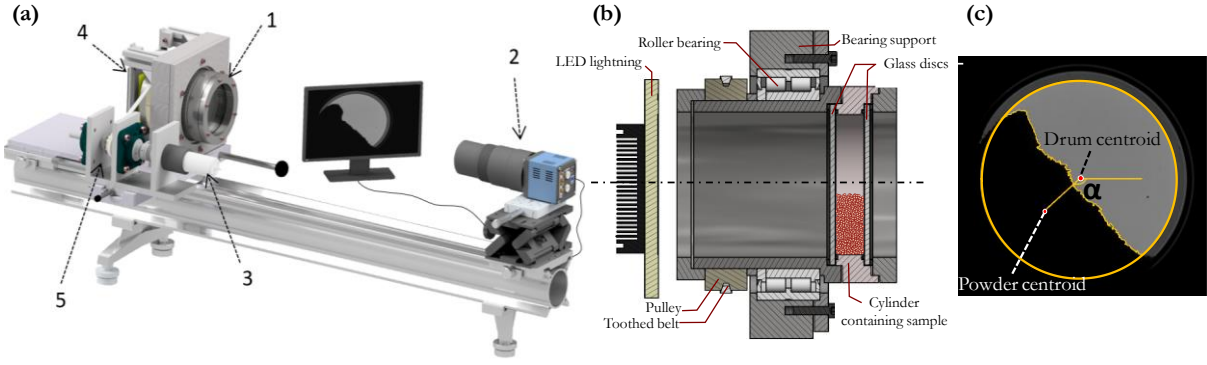
206 In order to observe and record powder motion, an optical montage ensuring axial alignment between  
207 the camera and the drum was built. Images were acquired using a *Photron FASTCAM* high-speed camera  
208 (*Mini AX100*, max. resolution 1 024 x 1 024 pixels, max. framerate 4 000 fps) along with a 105 mm f2.8 *EX*  
209 *DG Macro OS SIGMA* lens. A framerate of 50 fps during 1065 s with a resolution of 896×720 pixels was  
210 used. This configuration allows a relatively high exposure time (1/30 000 s) while taking clear images even  
211 during the avalanche motion. The camera was positioned horizontally facing the frontal side of the drum,  
212 with the center of view being aligned with the drum axis. A LED lighting panel (*HSC PHLOX 24 V*) was  
213 fixed behind the drum to obtain high-contrast shadow images of the powder.

214 A volume of 63 cm<sup>3</sup> of oven-dried materials was charged into the drum, corresponding to a filling ratio  
215 of 40 %. All the tests were performed at ambient relative humidity between 46 % and 55 % and at a  
216 rotational speed of 0.5 rpm. To automatically process the large set of images of each test (typically ca. 18.000  
217 images per test), a post-processing procedure was implemented using the Image Processing Toolbox™ of  
218 MATLAB platform.

219 Powder motion inside the drum was followed using the ‘centroid angle’ ( $\alpha$ ) defined as the angle between  
220 the horizontal and the line from center of the drum to the center of mass of the powder bed (Figure 2c).  
221 This indicator has been found relevant for the experimental evaluation of the flowability of cohesive  
222 materials using a rotating drum [25].

223 Three flow parameters were extracted from the temporal evolution of  $\alpha$ . The first one is the Upper  
224 Angle of Stability (*UAS*), which is defined as the maximum value of  $\alpha$  before an event (or ‘avalanche’). *UAS*  
225 is an indicator of the inter-particle frictional forces that particles must overcome to slide across over each  
226 other or to detach from the main bed to create an avalanche. Higher *UAS* values and wider *UAS*  
227 distributions generally correspond to a decreased flowability. The second one is the size of avalanches, that  
228 corresponds to the  $\alpha$  variation during an event. Large avalanches in cohesive materials are generally an  
229 indicator of poor flowability, as particles tend to form large clumps that break off and collapse over the  
230 powder surface. Finally, the third parameter is the fraction of revolution needed to trigger events (*f*), defined  
231 as  $f = \omega T / 60 \cdot 100 \%$ , where *T* is the time (s) between events and  $\omega$  is the rotational speed (rpm). A greater  
232 value of *f* normally indicates a greater powder cohesion since the events are less frequent. On the contrary,  
233 powders having small values of *f*-distributions should flow freely and require lower energy to trigger flow  
234 [19]. The determination coefficient ( $r^2$ ) was also calculated as an indicator of the smoothness of the free-  
235 surface profile of the powders. This coefficient evaluates the goodness of fit of a linear regression to the  
236 surface profile. Cohesive materials tend to form agglomerates when tumbling, so their surfaces are expected  
237 to be rough and irregular, resulting in values of  $r^2$  much less than the unit.

238



239  
 240 *Figure 2. Rotating drum system. (a) Experimental setup: 1: rotating cylinder, 2: high-speed camera, 3: motor, 4: lighting panel, 5. drive*  
 241 *system, (b) detail on the cylinder (c) Centroid angle ( $\alpha$ ) definition*

### 242 3. DEM modelling

243  
 244 This section starts with an overview of the DEM contact model used in this work and the procedure  
 245 for representing particle size and shape using a coarse-grained multisphere approach. Then, the  
 246 methodology for calibrating the DEM parameters is briefly explained and finally the geometry of the  
 247 simulated rotating drum is presented.

#### 248 3.1. Contact model

249 Simulations were conducted using the public version of LIGGGHTS 3.8.0 DEM code [68], parallelized  
 250 on a E5-2620 v4 2.10 GHz Intel® Xeon® machine with 125.8 GB of RAM. A classic non-linear spring-  
 251 dashpot model of Hertz-Mindlin was used as the basic contact model for all samples. For biomass samples,  
 252 an elastic-plastic spring-dashpot (EPSD2) rolling friction model and a simplified Johnson-Kendall-Roberts  
 253 (SJKR) cohesion model were also included.

254 The Hertz-Mindlin model stands as the most commonly used contact model due to its efficient and  
 255 accurate force calculations. At any time  $t$ , the equations governing the translational and rotational motion  
 256 of particle  $i$  of mass  $m_i$  and radius  $R_i$  can be written as:

$$257 \quad m_i \frac{d\mathbf{v}_i}{dt} = \sum_j (\mathbf{F}_{ij}^e + \mathbf{F}_{ij}^d + \mathbf{F}_{ij}^{coh}) + m_i \mathbf{g} \quad (2)$$

and

$$258 \quad I_i \frac{d\boldsymbol{\omega}_i}{dt} = \sum_j (\mathbf{T}_{ij}^t + \mathbf{T}_{ij}^r) \quad (3)$$

259 where  $\mathbf{v}_i$  and  $\boldsymbol{\omega}_i$  are the translational and rotational velocities of particle  $i$ .  $m_i$  and  $I_i$  are the mass and the  
 260 moment of inertia of the particle. The indices  $i$  and  $j$  can also represent particle-wall interactions. The forces  
 261 involved are: the gravitational force  $m_i \mathbf{g}$  and the forces between particles which include an elastic force  $\mathbf{F}_{ij}^e$   
 262 , a viscous damping component  $\mathbf{F}_{ij}^d$  and cohesive contributions (for biomass samples) through the  $\mathbf{F}_{ij}^{coh}$   
 263 term. The torque acting on particle  $i$  due to particle  $j$  includes two components:  $\mathbf{T}_{ij}^t$  which is generated by  
 264 the tangential force and causes particle  $i$  to rotate, and  $\mathbf{T}_{ij}^r$ , the rolling friction torque generated by  
 265 asymmetric distribution of the normal contact force and slows down the relative rotation between particles  
 266 in contact [69,70]. If particle  $i$  undergoes multiple interactions, the individual interaction forces and torques  
 267 sum up for all particles interacting with particle  $i$ . The equations for calculation of each force contribution  
 268 are reported in Table 2. A complete description of the elasto-plastic spring-dashpot rolling friction model  
 EPSD2 is given in [71].

269  
270

Table 2. Equations for calculations of forces and torques on particle  $i$  according to the Hertz-Mindlin model.

Force or torque contribution	Equation
Normal elastic force, $\mathbf{F}_{ij,n}^e$	$k_n \delta_{ij,n} = -\frac{4}{3} Y_{eff} \sqrt{R_{eff}} \delta_{ij,n}^{3/2}$
Normal damping force, $\mathbf{F}_{ij,n}^d$	$\gamma_n \mathbf{v}_{ij,n} = -\frac{2\sqrt{5/6} \ln(e)}{\sqrt{\ln^2(e) + \pi^2}} \sqrt{2Y_{eff} (R_{eff} \delta_{ij,n})^{1/2}} m_{eff} \mathbf{v}_{ij,n}$
Tangential elastic force, $\mathbf{F}_{ij,t}^e$	$k_t \delta_{ij,t} = -8G_{eff} \sqrt{R_{eff}} \delta_{ij,t}$
Tangential damping force, $\mathbf{F}_{ij,t}^d$	$\gamma_t \mathbf{v}_{ij,t} = -\frac{2\sqrt{5/6} \ln(e)}{\sqrt{\ln^2(e) + \pi^2}} \sqrt{8G_{eff} (R_{eff} \delta_{ij,t})^{1/2}} m_{eff} \mathbf{v}_{ij,t}$
Coulomb friction limit	$\delta_{ij,t}$ truncated to satisfy $\mathbf{F}_{ij,t}^e \leq \mu_s \left  \mathbf{F}_{ij,n}^e + \mathbf{F}_{ij,n}^d + \mathbf{F}_{ij,n}^{coh} \right $
Torque by tangential forces, $\mathbf{T}_{ij}^t$	$\mathbf{R}_{ij} \times (\mathbf{F}_{ij,t}^e + \mathbf{F}_{ij,t}^d)$
Torque by rolling friction, $\mathbf{T}_{ij}^r$	EPSD2 model

271 where  $\sqrt{1/m_{eff}} = \sqrt{1/m_i} + \sqrt{1/m_j}$ ,  $\sqrt{1/R_{eff}} = \sqrt{1/R_i} + \sqrt{1/R_j}$ ,  $\sqrt{1/\gamma_{eff}} = (1-\nu_i^2)/\gamma_i + (1-\nu_j^2)/\gamma_j$ ,  $\sqrt{1/G_{eff}} = 2(2-\nu_i)(1+\nu_i)/\gamma_i + 2(2-\nu_j)(1+\nu_j)/\gamma_j$ ,  $\mathbf{R}_{ij} = R_i(\mathbf{r}_j - \mathbf{r}_i) / (R_i + R_j)$ ,  
272  $e$ : coefficient of restitution,  $Y$ : Young's modulus,  $G$ : shear modulus,  $\nu$ : Poisson's ratio.

273 Cohesive force models in DEM include the Johnson, Kendall and Roberts (JKR) model [72], the  
274 recently developed Parallel Bond Contact Model [73] and Adhesive Elasto-Plastic Contact Models [74]. The  
275 simplified formulation of the widely-used Johnson-Kendall-Roberts model (sJKR) [75] was used in this  
276 work, for several reasons: (i) because of its availability in LIGGGHTS, (ii) the need for a single calibration  
277 parameter and (iii) the successful description of low-stress cohesive material flows that has been observed  
278 in previous research [46,59]. This model adds an additional normal force  $\mathbf{F}_{ij,n}^{coh}$  tending to maintain the  
279 contact between two particles, given by:

$$\mathbf{F}_{ij,n}^{coh} = CED \cdot \mathcal{A} \quad (4)$$

280 where  $CED$  is the Cohesive Energy Density in  $\text{J}/\text{m}^3$  and  $\mathcal{A}$  is the contact area between particles,  
281 calculated as:

$$\mathcal{A} = \frac{\pi}{4} \frac{(d_{ij} - R_i - R_j)(d_{ij} + R_i - R_j)(d_{ij} - R_i + R_j)(d_{ij} + R_i + R_j)}{d_{ij}^2} \quad (5)$$

282 where  $d_{ij}$  is the distance between the center of the particles and  $R_i$ ,  $R_j$  are the radii of the spheres  $i$  and  $j$   
283 in contact. For a particle ( $i$ )-wall ( $j$ ) contact, the contact area becomes:

$$\mathcal{A} = \pi(R_i^2 - d_{ij}^2) \quad (6)$$

284

### 285 3.2. Particle shape approximation

286

287 To simulate the elongated shape of the biomass particles, a multi-sphere approach was used [76]. Indeed,  
288 since spherical shapes facilitate computationally-efficient contact detection, the multi-sphere method is one  
289 of the most widely used approach for representing particle shape in DEM [45,77]. Spheres within a multi-  
290 sphere cluster are fixed in position relative to each other and may overlap to approximate more closely to  
291 the actual particle shape [76]. Multi-sphere representations have previously been used for describing flow  
292 of submillimetric biomass particles [59], wood chips [78] and agricultural resources such as maize and rice  
293 grains [79,80].

294 Each sample was simulated as a monodisperse population of multi-sphere clusters. High-quality  
 295 approximations of particle shape using a multisphere approach may require a large number of spheres,  
 296 making simulations very demanding in memory and computation time. To reduce the number of spheres  
 297 required to represent a single particle, the individual spheres were oriented on a single longitudinal axis, so  
 298 that the particles were needle-shaped (Figure 3). To approximate the actual morphology obtained by the  
 299 PSD measurements, a simplified model of particle representation was proposed. In this model, the number  
 300 of spheres in a clump,  $n_{spb}$ , is function of the particle mean size ( $d_{50}$ ), the average aspect ratio ( $a_{50}$ ) (Table 1)  
 301 and an overlapping factor  $c$ .

302 The overlapping factor is defined as  $c = \lambda / d_{50}$ , where  $\lambda$  is the overlapping distance between adjacent  
 303 spheres in  $\mu\text{m}$  (Figure 3a). A value of  $c = 0$  means that two spheres touch at one single point and  $c = 1$   
 304 represents a total overlap between two contiguous spheres. As  $c$  increases, the effective roughness of the  
 305 particle decreases. Previous work [77] has suggested that reducing surface roughness by increasing the  
 306 number of spheres per cluster does not necessarily lead to a better approximation of particle behavior. A  
 307 value of  $c$  of 20 % was chosen as it is considered a good trade-off between the accuracy of particle  
 308 representation and the number of spheres required.

309 The diameter of each sphere is set to be equal to the median minimum Feret diameter of the population,  
 310  $d_{50}$ . Therefore, the length of the clump ( $l_{clump}$ ), which corresponds to the average maximum Feret diameter,  
 311 can be calculated as follows:

$$l_{clump} = d_{50} / a_{50} = n_{spb} \times (d_{50} - \lambda) + \lambda \quad (7)$$

312 So, from the definitions of  $a_{50}$  and  $c$ , the number of spheres needed per clump is:

$$n_{spb} = \frac{1/a_{50} - c}{1 - c} \quad (8)$$

313 The calculated values were rounded to the closest integer and the length of the clump was  
 314 recalculated accordingly.

315 The volume of each clump is given by:

$$V_{clump} = n_{spb} \pi \left( \frac{d_{50}}{2} \right)^3 \left( \frac{4}{3} - \frac{n_{spb} - 1}{12n_{spb}} (6 - 2c)(4c^2) \right) \quad (9)$$

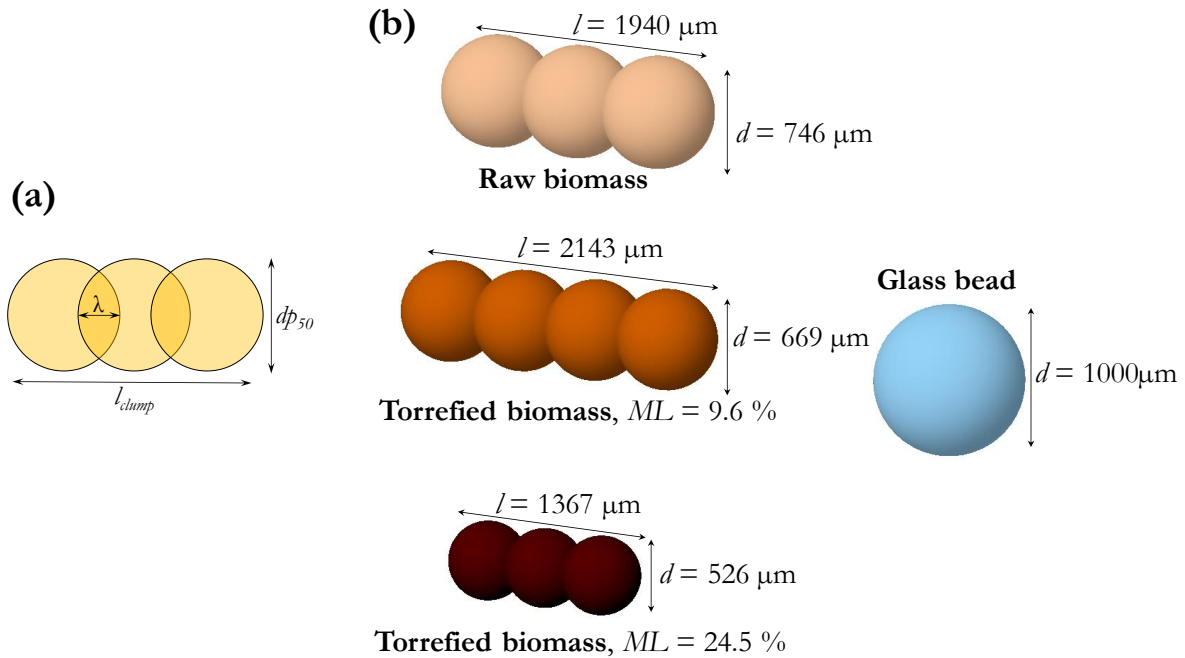
316 Table 3 shows the multisphere model parameters that define each sample. For the sake of  
 317 comparison with spherical models for particle representation, the equivalent diameter of a sphere having  
 318 the same volume as one individual clump ( $d_{eq}$ ) is also reported. Figure 3b presents the multisphere model of  
 319 each sample used in this investigation.

320

321 *Table 3. Characteristics of the multisphere model for representation of biomass particles (non-scaled).*

	Raw	ML = 9.6 %	ML = 24.5 %
$n_{spb}$	3	4	3
$l_{clump}$ ( $\mu\text{m}$ )	1940	2273	1367
$V_{clump}$ ( $\text{mm}^3$ )	0.6282	0.5997	0.2199
$d_{eq}$ ( $\mu\text{m}$ )	1062	1046	748

322



324

325

326

Figure 3. Multisphere particle representation. (a). Nomenclature of main dimensions within a multisphere clump. (b). Models of biomass samples and glass bead used in DEM simulations (non-scaled, true relative size).

327

328

### 3.3. Particle size upscaling and material model calibration

329

330

331

Using simplified shape representations of the actual particle shape is a common practice. However a realistic material behavior has to be ensured through calibration [81].

332

333

334

335

336

337

338

339

340

341

342

343

The material DEM model of biomass powders was calibrated using the procedure described in detail in [59,82]. Calibration of the inter-particle coefficients of sliding ( $\mu_s$ ) and rolling friction ( $\mu_r$ ) and the Cohesion energy density ( $CED$ ) was performed by comparing experimental bulk measurements against results of DEM simulations. The tested values for  $\mu_s$  and  $\mu_r$  varied between 0.1 and 0.9 and between 0 and 80 kJ/m<sup>3</sup> for the  $CED$  parameter. The bulk responses used were: angle-of-repose from a heap, bulk density and a shear box retainment ratio. The minimization of the discrepancy between numerical and experimental results was carried out using a Non-Dominate Sorting Genetic Algorithm (NSGA-II) [83], proven successful in previous research for DEM calibration [82]. Two objective functions were defined:  $O_1$ , the relative error between the simulated angle-of-repose and bulk density and the experimental values, and  $O_2$ , the relative error between the experimental and simulated shear ratio. The shear ratio corresponded to the ratio of the number of particles remaining inside a shear box after the outlet lid was lifted and the initial number of particles poured into the box.

344

345

346

347

348

349

According to the dimensions of the particle clumps reported in Table 3, to simulate the formation of a full heap, several hundreds of thousands of particles would have to be included in the simulation domain, which would require several weeks of computation. Consequently, a coarse-graining approach [54,55,57] was followed and a trade-off between the actual representation accuracy and the calculation effort was made by scaling particle size up by a factor of 4. This led to a computation time for a typical heap formation simulation of ca. 1 hour and ca. 1 week for the simulation of three drum rotations.

350 Following the procedure described in [59] led to a population of optimal possible combinations of  
351 parameters that adjusted well the physical responses obtained from bulk setups. Preliminary simulations  
352 showed that low values of  $CED$  (e.g. 10 kJ/m<sup>3</sup>) did not yield a qualitative cohesive behavior in the rotating  
353 drum simulations (revealed in the experiment by an irregular powder surface or the generation of particle  
354 agglomerates) for the raw biomass sample. Similar observations have been made by Nasato et al. [55] where  
355 too low cohesive forces in simulations of a shear test led to an identical flow behavior of a non-cohesive  
356 Hertz contact model. Therefore, the values of  $\mu_s$ ,  $\mu_r$  and  $CED$  used for rotating drum simulations (Table 4)  
357 were selected among the optimal parameter sets with the highest values of  $CED$  [59]. Values for glass beads  
358 reported in Table 4 were taken from [84]. Except for  $CED$ , particle-walls interaction parameters were set  
359 based on literature values for woody materials [81,85]. In line with previous research [86,87], particle-steel  
360  $CED$  was set at half the value of the interparticle  $CED$ .

361

362 *Table 4. DEM simulation parameters for particles and walls.*

Parameter	Glass beads	Raw biomass	Torrefied $ML = 9.6\%$	Torrefied $ML = 24.5\%$
Poisson's ratio (particle-particle)	0.22	0.3	0.3	0.3
Poisson's ratio (particle-walls)	0.22	0.3	0.3	0.3
Particle density, kg/m <sup>3</sup>	2550	350	350	350
Young's modulus (particle-particle), Pa	$5 \times 10^6$	$5 \times 10^6$	$5 \times 10^6$	$5 \times 10^6$
Young's modulus (particle-walls), Pa	$5 \times 10^6$	$5 \times 10^6$	$5 \times 10^6$	$5 \times 10^6$
Coefficient of restitution (particle-particle)	0.87	0.1	0.1	0.1
Coefficient of restitution (particle-walls)	0.87	0.1	0.1	0.1
Sliding friction coefficient (particle-particle)	0.2	0.1	0.3	0.693
Sliding friction coefficient (particle-steel)	0.6	0.4	0.4	0.4
Sliding friction coefficient (particle-glass)	0.2	0.5	0.5	0.5
Rolling friction coefficient (particle-particle)	----	0.7	0.3	0.131
Rolling friction coefficient (particle-walls)	----	0.5	0.5	0.5
Cohesion Energy Density (particle-particle), J/m <sup>3</sup>	----	50 049	77 576	79 062
Cohesion Energy Density (particle-steel), J/m <sup>3</sup>	----	25 024	38 788	39 531
Time-step (s)	$1.5 \times 10^{-5}$	$1 \times 10^{-5}$	$1.5 \times 10^{-5}$	$1 \times 10^{-5}$
Total number of spheres	19 791	39 366	34 288	72 816
Number of clumps	----	13 122	8 572	24 272
Number of processors	8	2	4	8

363

364

365

### 3.4. Simulated system description

The upscaled calibrated particle models were first used in simulations of the rotating drum at its actual dimensions. However, due to the upscaled particle size, very few grains were included in the domain when the real cylinder dimensions were used in simulations. This, combined with the resulting very high wall effects, prompted us to scale the cylinder dimensions up by a factor of 4 (i.e. to use an ‘exact scaling’ approach [41,53,88]). Although the use of an exact scaling approach offers no advantage regarding the simulation time, it provides a sufficient number of particles in the simulation domain to reproduce a macroscopic bulk behaviour of the material. Considering the large number of particles to be simulated, the application of a periodic boundary conditions (PBC) approach was explored on a preliminary basis.

Indeed, besides particle size scaling, another approach commonly used to increase computational efficiency in symmetric axial geometries such as cylinders, is to apply periodic boundary conditions in the axial direction [89]. This approach considers the bed of particles as an infinite array of identical translated layers of itself. Particles exiting one end of an axial boundary re-enter at the opposite boundary. Therefore, the effects of the endplates are not considered and only a thinner slice representing the center of the drum needs to be simulated, which could drastically reduce the computing time compared to the full system.

A cylindrical slice of the drum of 20 mm wide and 400 mm in diameter was used for PBC simulations. This width (axial dimension) of the disc corresponded to  $\frac{1}{4}$  of the scaled width. Figure 4 shows a comparison between experimental images for a biomass sample and glass beads (Figure 4a and d), snapshots of the corresponding simulations using PBC (Figure 4b and e) and images using a closed geometry with the same width and endplates (Figure 4c and f). The behavior obtained from DEM simulations with PBC did not correspond to the experimental observations: in the case of the glass bead samples, a slumping rather than a continuous regime developed [16], while for biomass samples, the powder collapsed on itself at very low  $\alpha$  angles. Simulations using glass endplates reproduced better the experimental behavior displaying correct qualitative features: a continuous flow regime with a constant slope developed for glass beads and high-potential avalanches took place for biomass. This shows that the inclusion of wall friction effects is required to simulate a realistic flow. Therefore, the final simulated drum configuration included these endplates.

The main drum dimensions used for simulations are presented in Table 5. It should be noted that to reduce computing time, the cylinder width used for PBC simulations was kept in the finally simulated system. The number of particles between endplates for the elongated biomass samples ( $n$ ) is calculated based on the equivalent diameter of the clumps  $n=w/(d_{eq}\times 4)$  (Table 3). The values of  $n$  were in all cases above 4. Johnstone [43] reported that four particles between the endplates were a good compromise between computational time requirement and the accuracy of the dynamic angle determination. For each sample, the number of particles to achieve a 40 % fill volume is also reported in Table 5. The values for biomass samples correspond to the number of elongated clumps, so the total number of simulated individual spheres correspond to the value reported in Table 5 multiplied by the number of spheres per clump.

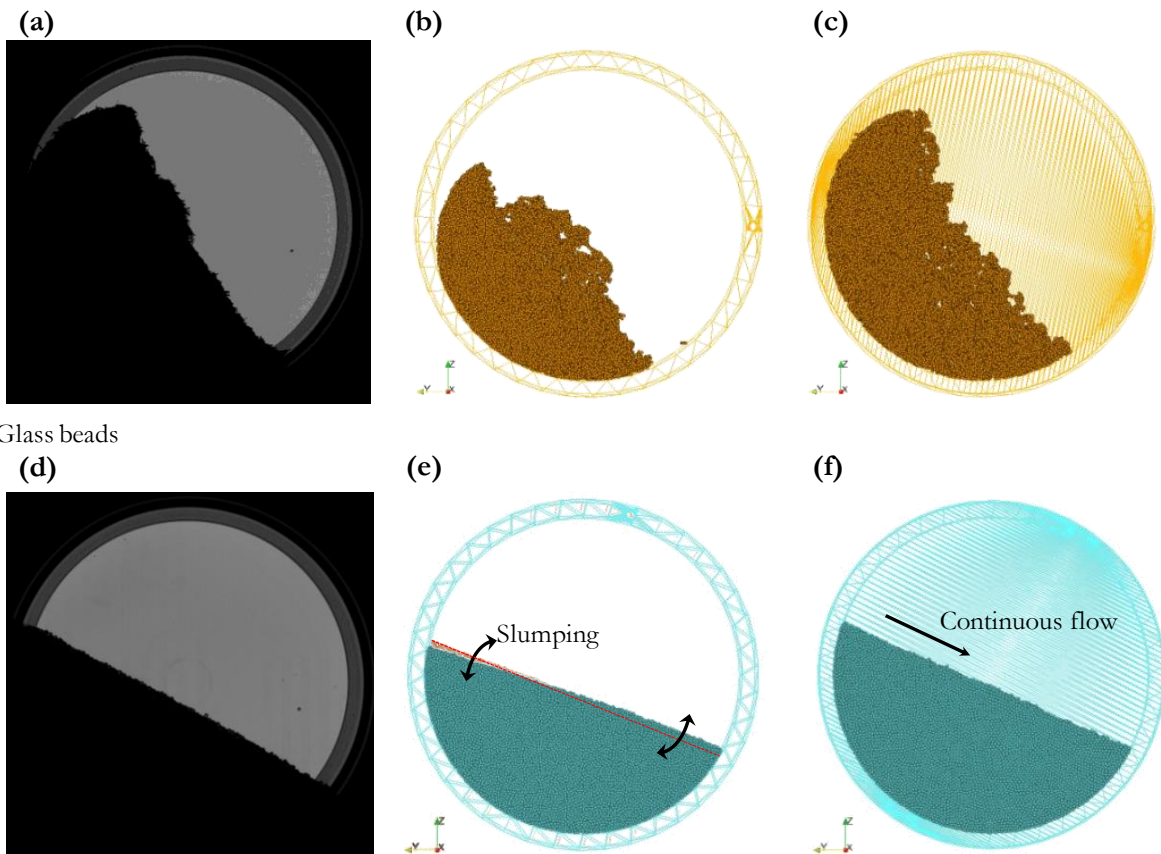
As in experiments, the rotational speed of the drum was 0.5 rpm. The randomly-oriented particles were inserted into the cylinder volume and allowed to settle for 10 000 timesteps. Previous research by Marigo [52] on cohesionless alumina cylindrical pellets has shown that a steady-state could be achieved after one rotation while DEM simulations of plastic balls by Liu et al. [90] needed at least two rotations to reach steady state. Mishra et al. [46] reported the attainment of a steady-state for agglomeration of cohesive particles inside a rotating drum after 1.5 revolutions of the drum. In this work, simulations were conducted for a duration equivalent to 3 drum rotations (360 s).

411 *Table 5. Characteristics of the simulated rotating drum system.*

Drum diameter	Glass beads	100 mm
	Biomass samples	400 mm
Drum width ( $w$ )	Glass beads	5 mm
	Biomass samples	20 mm
Number of particles between endplates ( $w/d_{eq}$ )	Glass beads	5
	Raw biomass	4.7
	Torrefied, $ML=9.6\%$	4.8
	Torrefied, $ML=24.5\%$	6.7
Number of elongated clumps in domain	Glass beads	19 791
	Raw biomass	19 376
	Torrefied, $ML=9.6\%$	8 572
	Torrefied, $ML=24.5\%$	24 272

412  
413  
414  
415  
416

Torrefied biomass,  $ML = 24.5\%$



417  
418  
419  
420  
421

Figure 4. Experimental and DEM-simulated motion inside the rotating drum for torrefied biomass and glass beads samples. (a,d). Experimental images. (b,e). DEM simulation snapshots using PBC. (c,f). DEM simulations with endplates.

## 4. RESULTS AND DISCUSSION

In this section, comparisons between the experimental behavior and DEM simulations are made, firstly, based on the visual observations of the material motion and then from quantitative flowability indicators. The experimental results presented here have been thoroughly discussed in [66] so that the analysis hereafter focuses on the description of the numerical results and their comparison with the observed experimental behavior.

Figure 5 shows a qualitative comparison between representative experimental and simulation captions after avalanches. Visually, the similarities between the simulation and the experimental results are encouraging. Overall, the differences in behavior between the different samples studied here are well captured by the DEM simulations.

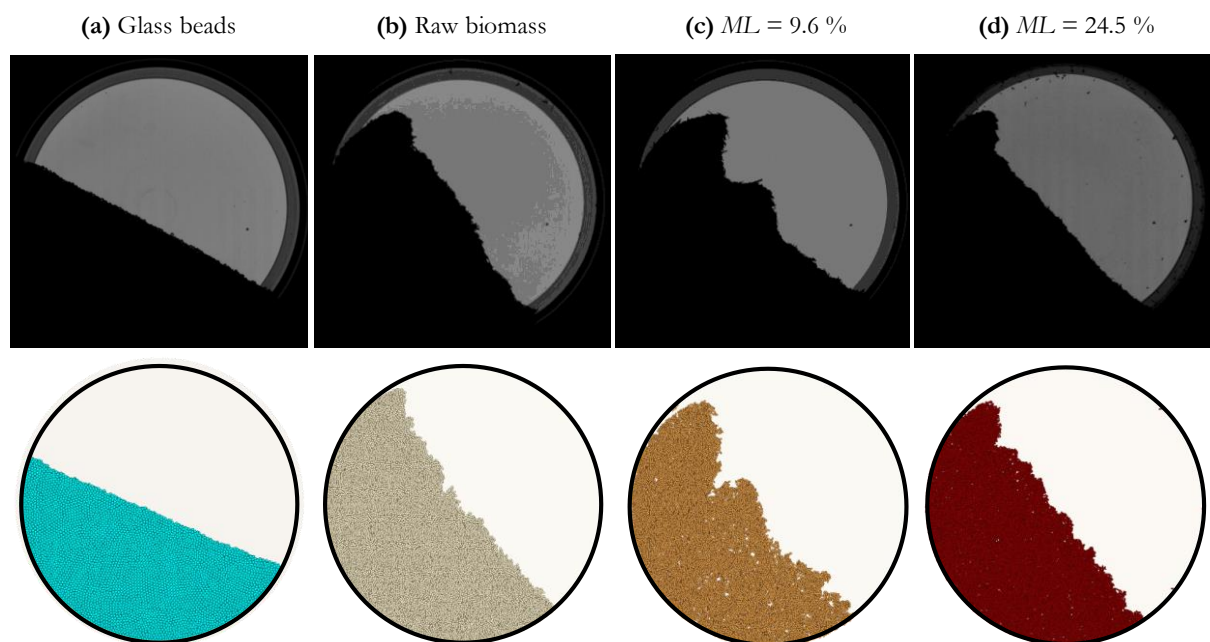


Figure 5. Typical experimental and simulated post-avalanche profiles after one rotation.

Both experimentally and numerically, a continuous regime of flow develops for glass beads with little variations of the flat free-surface slope. For biomass samples, qualitatively, the motion of the powder bed occurs in the form of intermittent collapses of particle clusters, which is a characteristic behavior of cohesive materials [21]. This led to irregular free-surface profiles after avalanches that are well reproduced by simulations. This behavior is more pronounced for the mildly torrefied sample (Figure 5c), for which very rugged and irregular profiles are observed. In all cases, simulations led to a higher roughness of the free-surface than that observed in experiments. A higher apparent porosity of the powder bed compared to experiments is also visible in the simulations, which is likely to be mainly a visualization effect, since the width of the simulated drum (i.e. the number of axially superposed particles) was reduced compared to the real setup.

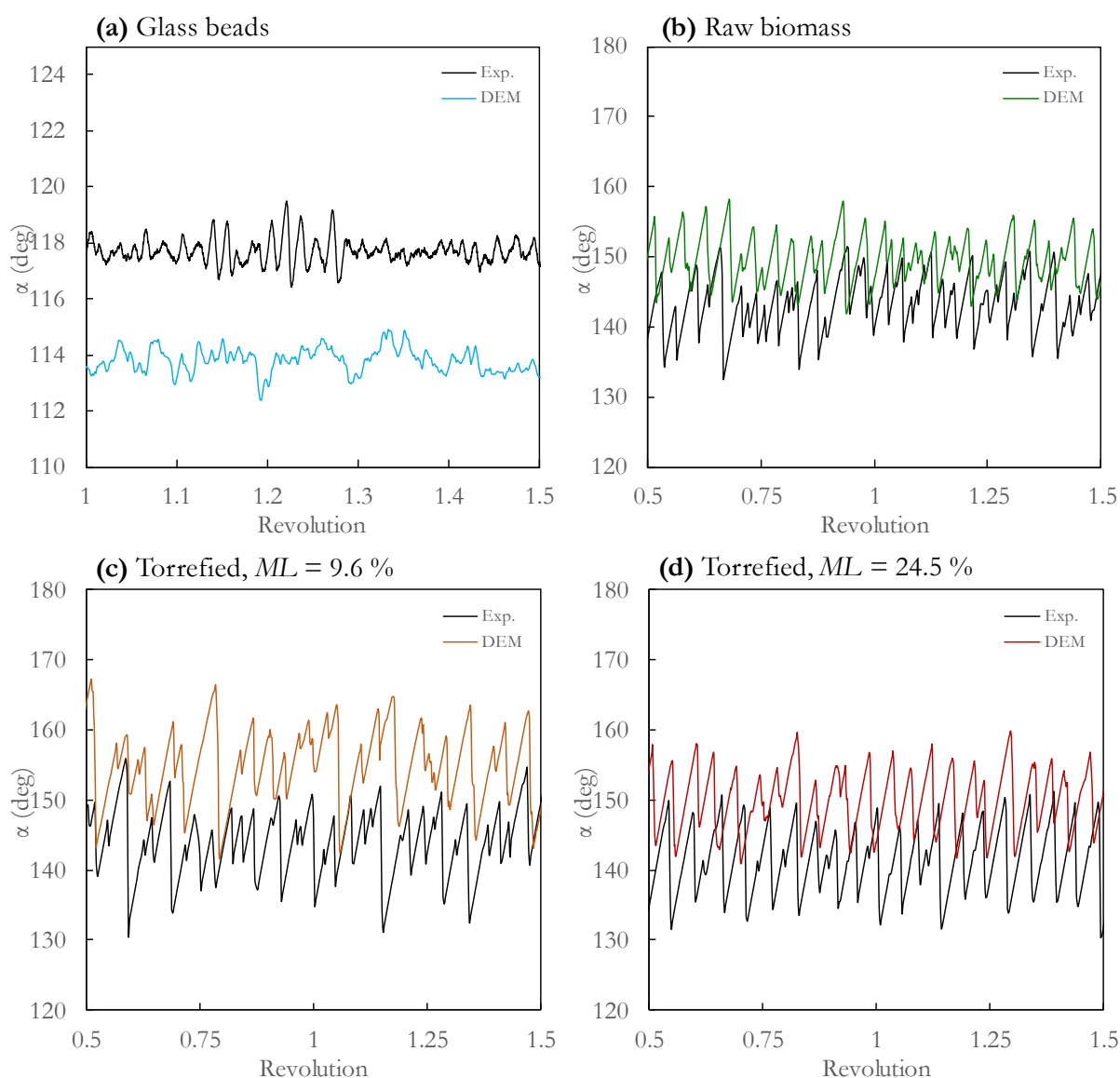
The temporal evolution of the centroid angle  $\alpha$  during one drum rotation is shown Figure 6. Numerically, for glass beads, it took 8 % of rotation to trigger the first avalanche, while for biomass powders around 20 % of a rotation was needed. After the first avalanche, both numerically and experimentally, there

450 is no clear evolution towards a steady-state in terms of the centroid angle, so the segments showed in Figure  
451 6 can be considered as qualitatively representative of the entire simulated period (3 drum rotations).

452 The qualitative behavior of the four samples in terms of  $\alpha$  evolution was well reproduced by simulations.  
453 Both numerically and experimentally, for glass beads, there are very rapid and very short variations of  $\alpha$  of  
454 up to  $2^\circ$  while, for biomass, there is a succession of large quasiperiodic events consisting in decreases of  $\alpha$   
455 of up to  $20^\circ$ . Small random events are also common for the simulations of both raw and mildly torrefied  
456 biomass (Figure 6b and c) while a more regular pattern of large events (nearly uniform in size and time  
457 spacing) is visible for the intensively torrefied sample (Figure 6c). Quantitatively, it is however apparent  
458 from Figure 6 that there is an evident minor quantitative gap between experimental results and simulations.

459 The flowability parameters explained in Section 2.2 were evaluated from the experimental and  
460 simulation results and used to quantitatively differentiate the cohesiveness of the different powders.

461



462  
463 *Figure 6. Experimental and DEM-modelled evolution of the 'centroid angle'. The x-axis ('Revolution') is the fraction of rotation (i.e. the*  
464 *product between the rotational speed and the elapsed time in homogeneous units).*

465 Because of the highly variable profiles shown in Figure 6, the flowability parameters are presented in  
466 Figure 8 in terms of occurrence distributions rather than simply as average values. The median values of the

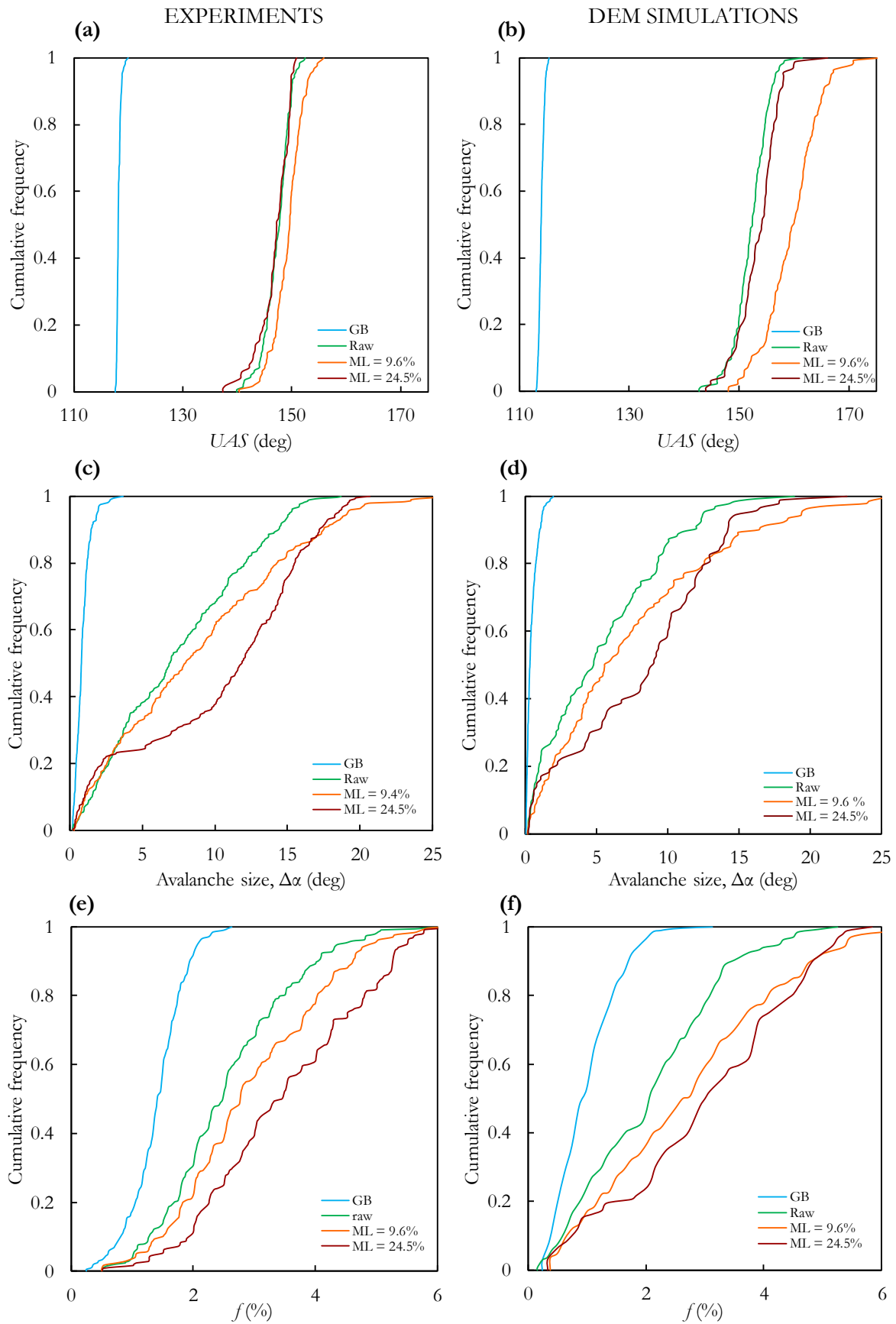
467 distributions (50<sup>th</sup> centile) are reported in Table 6 and used to establish flowability rankings. Quantitatively,  
468 the width of the distributions for a given flowability parameter ‘ $\varepsilon$ ’ is quantified by the span  $S_\varepsilon$ , calculated as  
469 follows:

$$S_\varepsilon = \frac{\varepsilon_{90} - \varepsilon_{10}}{\varepsilon_{90} + \varepsilon_{10}} \quad (10)$$

470 where  $\varepsilon_{90}$  and  $\varepsilon_{10}$  are the 90<sup>th</sup> and 10<sup>th</sup> centiles of the cumulative  $\varepsilon$ -distributions, respectively.

471 Figure 7 shows the cumulative distributions for the upper angle of stability obtained from the  
472 experimental results (Figure 7a) and the DEM simulations (Figure 7b). Overall, the behavior for simulations  
473 and experiments in terms of  $UAS$  is similar: a very steep unimodal distribution is obtained for the glass  
474 beads, around a value a few tens of degrees lower than that of biomass powders, which is indicator of a  
475 free-flowing behavior. In the case of the biomass powders, the distributions spread over a wider range of  
476 values, as can be expected from the plots in Figure 6. The raw and the intensively torrefied samples exhibit  
477 very close  $UAS$  distributions, while the mildly torrefied samples have greater  $UAS$  values, indicating a higher  
478 cohesive nature.

479 In addition to interparticle interactions, the moment at which particles detach from the drum walls is  
480 likely to be strongly influenced by the wall-particle particle-wall interactions, namely the coefficients of  
481 friction and the cohesion energy. These parameters were not considered in the calibration framework  
482 (Section 3.3). This might explain the quantitative offset of the DEM distributions compared to the  
483 experimental results. Nevertheless, results of Table 6 for  $UAS$  show that DEM simulations predicted within  
484 a low margin of error (below 7 %) the experimental values.



485  
486  
487

Figure 7. Distributions of flowability descriptors. Left-side plots correspond to the experimental results, right-side are the results obtained from DEM simulations. (a,b) UAS. (c,d) Avalanche size. (e,f) Fraction of revolution needed to trigger events.

488 Figure 7c-d compares the experimental and simulated avalanche size ( $\Delta\alpha$ ) distributions. While very short  
489 avalanches were observed for glass beads, which is characteristic of a non-cohesive material, large angle  
490 variations during events were observed for the biomass powders. These large variations of  $\alpha$  are produced  
491 by the tumbling of clusters of particles, measured experimentally and nicely reproduced numerically, which  
492 rapidly modify the center of mass of the powder bed. While the qualitative similarity between the plots in  
493 Figure 7 is encouraging, the average avalanche size (Table 6) was always underestimated by the DEM  
494 simulations. However, the same experimental and numerical ranking of flowability could be established.

495

496 *Table 6. Experimental and simulated results for several flowability indicators. Span values (Eq. 10) are indicated in round brackets,*  
497 *flowability ranking is reported in square brackets from I being the worst flowing material to IV the material with the best flowability. The*  
498 *relative error is referred to as e.*

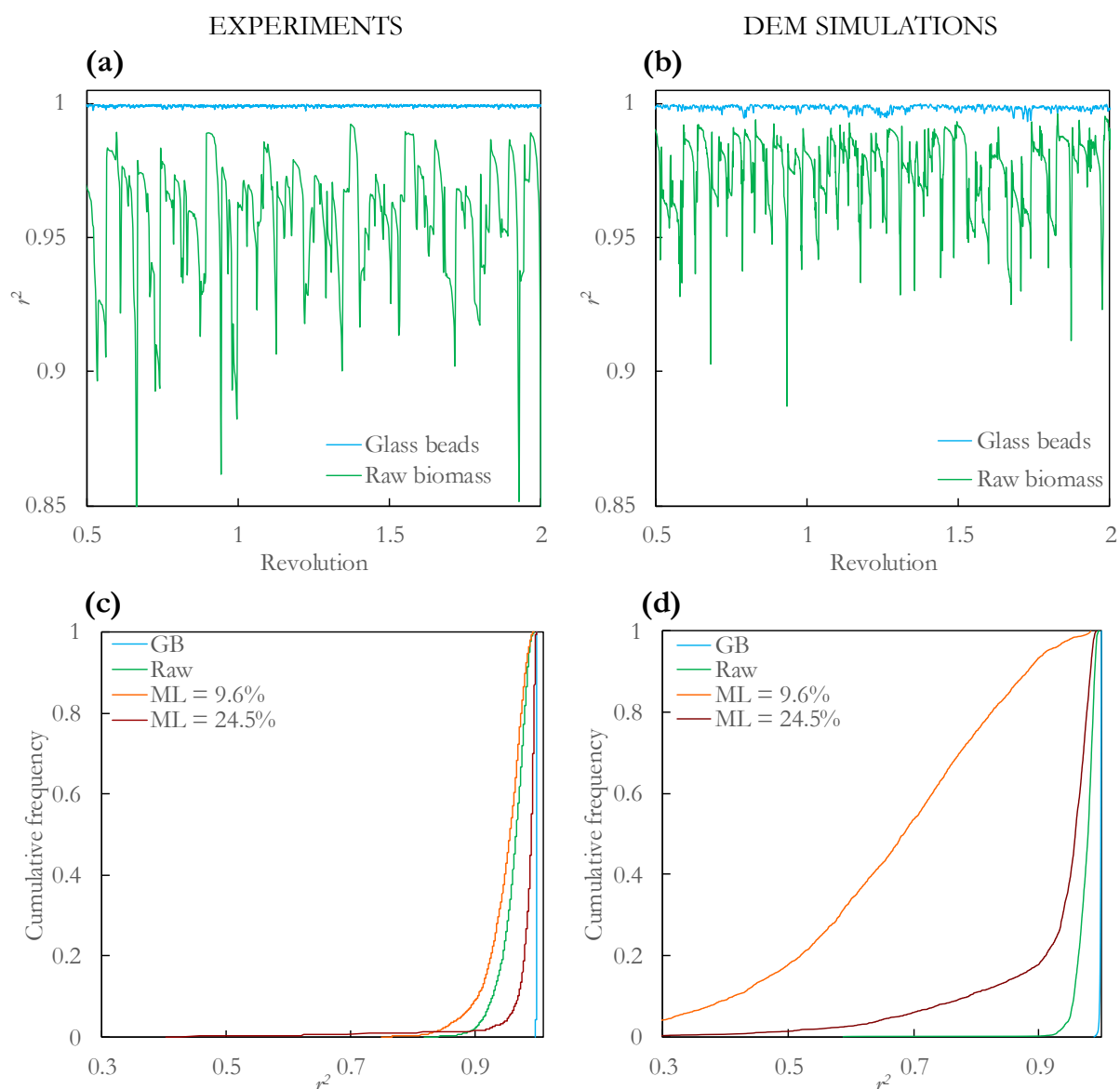
Sample	$UAS_{50}$ ( $S_{UAS}$ ) (deg)			Avalanche size $\Delta\alpha$ (deg)			$f_{50}$ ( $S_f$ ) (%)			$r^2_{50}$ ( $S_r^2$ )		
	Exp.	DEM	e (%)	Exp.	DEM	e (%)	Exp.	DEM	e (%)	Exp.	DEM	e (%)
Glass beads	118.1 (0.004) [IV]	114.0 (0.006) [IV]	3.5	0.81 (0.64) [IV]	0.32 (0.85) [IV]	60.5	1.41 (0.42) [IV]	0.93 (0.63) [IV]	34.0	0.999 (0.00) [IV]	1.00 (0.00) [IV]	0.1
Raw biomass	147.7 (0.02) [II]	152.4 (0.024) [III]	3.2	6.84 (0.80) [III]	4.79 (0.92) [III]	30.0	2.48 (0.52) [III]	2.06 (0.71) [III]	16.9	0.966 (0.030) [II]	0.98 (0.02) [III]	1.5
Torrefied, $ML=9.6\%$	149.6 (0.02) [I]	159.8 (0.041) [I]	6.8	7.98 (0.88) [II]	5.61 (0.90) [II]	29.7	2.77 (0.51) [II]	2.62 (0.76) [II]	5.5	0.956 (0.040) [I]	0.68 (0.36) [I]	28.9
Torrefied $ML=24.5\%$	147.2 (0.02) [III]	154.1 (0.03) [II]	4.7	11.8 (0.89) [I]	8.88 (0.93) [I]	24.7	3.44 (0.46) [I]	3.00 (0.74) [I]	12.8	0.991 (0.014) [III]	0.96 (0.11) [II]	3.13

499

500 Similar observations can be made from Figure 7e-f regarding the fraction of revolution  $f$  needed to  
501 trigger events. Again, lower fractions were obtained for glass beads, indicating a greater ease of flow. For  
502 the biomass samples, events required a larger fraction of revolution to occur, i.e. they were triggered less  
503 frequently, which is an indicator of a reduced flowability. Qualitatively, the shape and locations of the  
504 simulated  $f$ -distributions were consistent with the experimental results. Lower discrepancies between the  
505 average simulated and the experimental values of  $f$  were obtained for the biomass materials than for the  
506 glass beads (Table 6), and the same flowability ranking as in the experiments could be established. Intensively  
507 torrefied samples were less prone to flow in terms of event frequency, followed by the mildly torrefied  
508 sample, the raw sample and finally the non-cohesive glass beads. A comprehensive critical analysis on the  
509 use of the  $f$  parameter as indicator of flowability has been made in previous research [91]. The identification  
510 of the type of events is also important to conclude on flowability when using this indicator. For the  
511 intensively torrefied samples, even if the events are more spaced over time, the representations in Figure 6d  
512 show that there are fewer ‘small’ events for these materials than for the mildly torrefied or the raw samples.  
513 These small events were associated to small clumps breakings over the powder bed, which are typical of a  
514 cohesive flow. Experimentally, the flow of the intensively torrefied samples was dominated by ‘large’ shear-  
515 flow events rather than ‘small’ clumps breaks. This behavior was also verified by visual observation of the  
516 simulation output. This highlights the importance of considering the type of motion taking place during  
517 avalanches, and not only isolated numerical indicators of the event frequency or size.

518 The evaluation of the coefficient of determination ( $r^2$ ) completes the analysis of flowability by examining  
519 the irregularity of the free-surface profile of the powder. Figure 8a-b correspond to the evolution of  $r^2$   
520 obtained from experiments and simulations for the glass beads and the raw biomass sample. While for the  
521 glass beads the values of  $r^2$  are nearly constant at ca. 1, for the biomass powder great deviations from a linear

522 profile develop, especially during avalanches. The very distinct behavior between the non-cohesive and the  
 523 cohesive materials was well reproduced by simulations as can be seen in Figure 8: a high irregularity was  
 524 observed for the biomass sample compared to the glass beads.



525  
 526 *Figure 8. Irregularity of the free-surface profile as measured by the coefficient of determination ( $r^2$ ). (a) Experimental evolution for raw*  
 527 *biomass and glass beads. (b) Simulated evolution for raw biomass and glass beads. (c) Experimental  $r^2$ -distributions. (d)  $r^2$ -distributions*  
 528 *from simulation results*

529 The cumulative distributions in Figure 8c-d were derived from the evolution of  $r^2$  over time. The  
 530 comparison of experimental and simulated distributions reveals rather significant differences. The coarse  
 531 grained model of particles led to powder beds with a free surface profiles that were ‘rougher’ than in  
 532 experiments. An overestimation of the cohesive strength (i.e. the *CED* values in the DEM models) could  
 533 also trigger more irregular profiles as a more cohesive behavior develops compared to the experimental  
 534 behavior. This can be seen in Figure 6 where the evolution of the centroid for the biomass powders is  
 535 always higher than the experimental trends. A finer calibration of the *CED* value, that appears to have a  
 536 significant impact on the flow patterns may be recommended.

537 Most striking are the significantly low values of  $r^2$  obtained for the mildly torrefied samples from  
 538 simulations. This is the combined result of the high *CED* value for this sample and its higher elongation

539 that led to very rough and irregular profiles. Except for for mildly torrefied samples, the average values of  
540  $r^2$  were similar in simulations and in experiments (Table 6) and were used to establish a flowability ranking,  
541 with the mildly torrefied sample exhibiting the most cohesive behavior and the glass beads being non-  
542 cohesive.

543 For all criteria, differences in the behavior showed between simulations and experiments are also likely  
544 to be the effect of the reduced number of events considered to draw the distributions from simulations.  
545 Indeed, in the experiments, distributions are calculated on the basis of about 3 times the number of events  
546 recorded for simulations (e.g. 145 events for raw biomass). Although the study of the effect of the number  
547 of events on the distributions obtained from simulations remains a concern of ongoing work, longer  
548 simulations would likely reduce experimental-DEM gaps.

549 One avenue left unexplored in this work is the relative cohesive strength of interaction of particles with  
550 the drum walls, which may have a strong influence on the powder motion (in particular the moment when  
551 particles detach from the walls). Further investigation and experimentation might evaluate calibration of  
552 particle-wall interaction parameters and their effects on the bulk flow.

553 The results presented here suggest that calibrated DEM parameters obtained from relatively easy-to-  
554 implement bulk setups (angle-of-repose, bulk density and a retainment ratio) could be used to reproduce a  
555 realistic dynamic non-consolidated flow of biomass particles. One might consider directly applying a  
556 calibration framework such as the one presented in [59] using rotating drum simulations and experiments  
557 to better adjust powder dynamic behavior. However, as highlighted by Hu et al. [27] and as noted in this  
558 work, the long computation time that would be required for calibration using indicators from a rotating  
559 drum makes this strategy impractical at present. Instead, the results obtained from avalanche assessment in  
560 rotating drums could be dedicated to narrow the population of optimal sets of parameters obtained from  
561 bulk experiments, with fewer/shorter simulations required. This leads to a more realistic and robust DEM  
562 material model and to a better representation of flow behavior under a wide range of flow conditions.

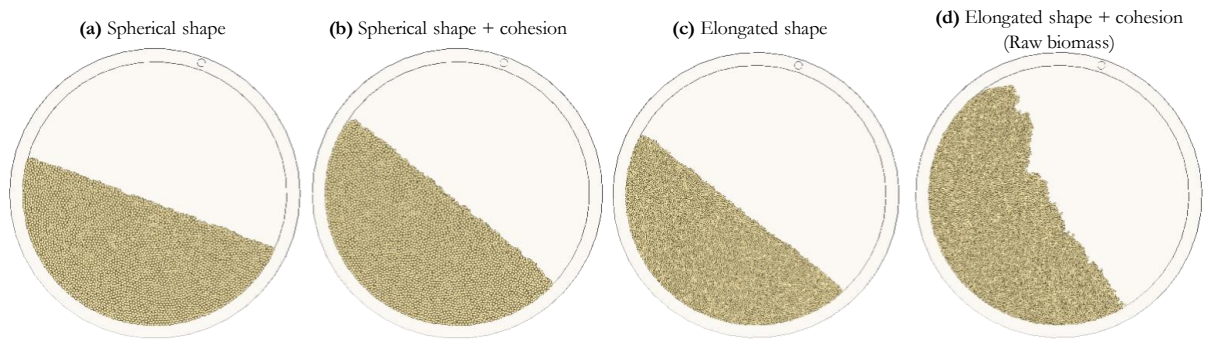
563

## 564 5. Potential of DEM simulations for exploration of shape and 565 cohesion effects on flow 566

567 The previous results proved that DEM simulations are capable of representing a realistic bulk flow of  
568 biomass particles under dynamic free-surface conditions. One of the greatest strengths of the simulation  
569 approach is that it allows the effect of the powder characteristics such as particle size, shape or interparticle  
570 cohesion on bulk flow to be studied independently. An overview of this potential is given hereinafter.

571 Figure 9 shows simulation snapshots that illustrate the effect of changes in particle properties (shape  
572 and cohesion) on the powder profile. Figure 9a corresponds to non-cohesive spherical particles with an  
573 equivalent diameter equal to that of the raw biomass scaled clumps ( $d_{eq} = 2.12$  mm), all the other DEM  
574 parameters being the same than those used for raw biomass simulations. Figure 9b shows the effect of  
575 adding a cohesive contribution of  $CED = 50.049$  kJ/m<sup>3</sup> (i.e.  $CED$  for raw biomass particles reported in  
576 Table 4.). In Figure 9c the elongated shape of the raw biomass clumps is used but interparticle cohesive  
577 forces are neglected and Figure 9d corresponds to the simulated raw biomass sample with the parameters  
578 of Table 4.

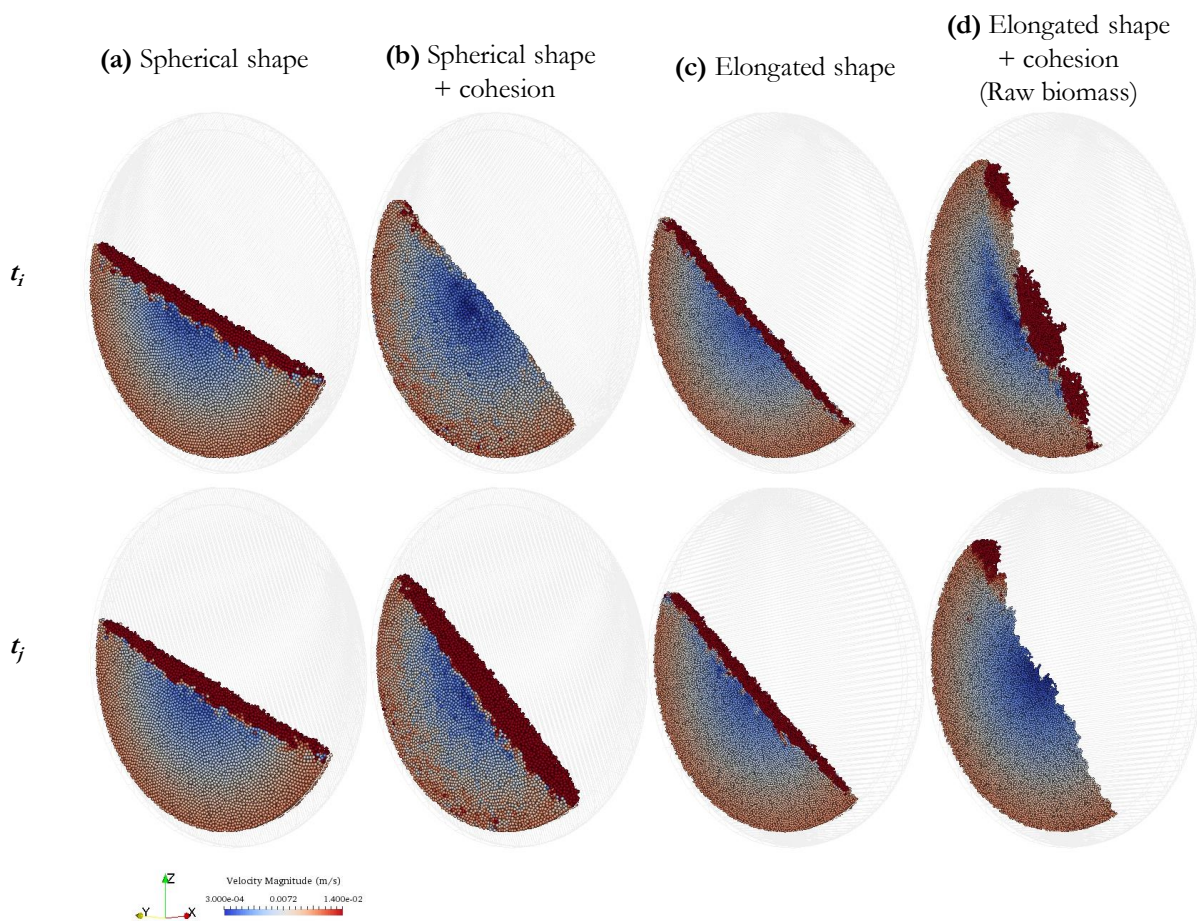
579  
580



581  
582

Figure 9. Snapshots of DEM simulations showing the effect of particle shape and interparticle cohesion on flow.

583 To facilitate the visualization of the dynamic flow behavior, snapshots of the flow with particles colored  
584 according to their instantaneous speed are presented in Figure 10 for two successive moments at  $t_i$  and  $t_j$ .  
585 The ease of access to detailed information at the particle-scale highlighted by the representations in Figure  
586 10 shows another interesting feature of DEM simulations. Figure 11 presents the evolution of the centroid  
587 angle during one rotation for the four cases presented in Figure 9 and Figure 10.



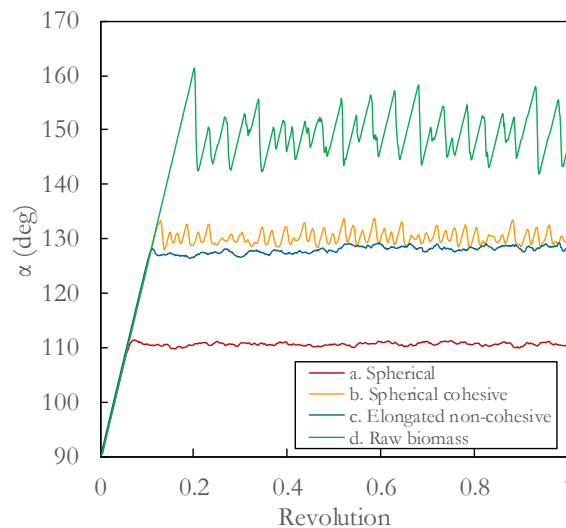
588  
589  
590  
591

Figure 10. Effect of particle characteristics on the flow behavior at two different moments. The time interval between  $t_i$  and  $t_j$  is generally the avalanche duration for the different material models, i.e. between 0.3 and 0.7 seconds. A similar time interval (c.a. 0.5 s) was used for the snapshots of models where a continuous regime developed (case a and c).

592

593 The lowest values of  $\alpha$  were obtained for the non-cohesive spherical particles and, as for the glass beads,  
 594 a continuous regime of flow developed with a flat and constant slope and a permanent layer of spheres  
 595 rolling down the free-surface (Figure 10a). Adding a cohesive contribution not only increased the centroid  
 596 angle (Figure 9b), but also resulted in a slumping regime in which periodic events took place: the solid bed  
 597 was lifted (Figure 10b, top) and leveled off (Figure 10b, bottom) by successive small discrete avalanches at  
 598 the surface.

599 Elongated shape promotes particle interlocking while limiting their free movement, which results in  
 600 greater centroid angles than for spherical particles (Figure 9c). Equivalent results for the dynamic angle of  
 601 repose are reported in previous research by Höhner et al. [39] and Wachs et al. [42]. Interestingly, without  
 602 cohesive interactions, a continuous regime of flow develops as in the case of the spherical particles.  
 603 Elongated particles simply shift the mean angle towards a higher value and the thickness of the shear front  
 604 of particles continuously flowing over the powder bed decreases (Figure 10c). Figure 11 shows that the  
 605 increase in the centroid angle triggered by the addition of cohesion (case b) or by an elongated shape (case  
 606 c) is, in average, comparable (ca.  $+20^\circ$  compared to the simulation of spherical particles). The difference  
 607 between these two cases is the presence of short oscillations when a cohesive contribution is taken into  
 608 account. Therefore, if only an average value of  $\alpha$  had been considered for flowability characterization (as is  
 609 often the case in literature), similar conclusions about flow would have been wrongly drawn for both cases.  
 610 This underlines the importance of considering several flow indicators in addition to average angles.



611  
 612 *Figure 11. Effect of particle characteristics on the temporal evolution of  $\alpha$  during one drum revolution.*

613 As seen in Figure 9d, only the coupled effects of the elongated particle shape and the interparticle  
 614 cohesion were able to reproduce a realistic behavior for the raw biomass samples, with discrete avalanches  
 615 (Figure 10d top) and the formation of clusters of particles collapsing over the free-surface. This triggered  
 616 the large  $\alpha$  variations depicted in Figure 11 that closely mimic the experimental behavior.

617 In this study, only monodispersed populations of particles were used in the simulations. However,  
 618 experimentally, although a sieving stage reduced the polydispersity of the biomass powders, there was still  
 619 a variety of particle sizes, especially for the intensively torrefied samples, which is likely to influence flow  
 620 behavior. A natural progression of this work is to analyze the effect of polydispersity on flow behavior  
 621 through simulations. Although this will be the subject of future research, a first effort in this direction is  
 622 shown here by simulating a polydispersed population with characteristics approximated from the PSD of  
 623 the raw biomass sample. Thus, three particle sizes at  $d_{8.2}$  (500  $\mu\text{m}$ ),  $d_{50}$  (746  $\mu\text{m}$ ) and  $d_{75}$  (890  $\mu\text{m}$ ) were  
 624 combined with volume proportions of 25 %, 50 % and 25 %, respectively, maintaining the same average  
 625 aspect ratio as the monodispersed system. As shown in Figure 12, the inclusion of two additional particle

626 sizes did not significantly change the bulk behavior in terms of the centroid angle evolution. Similar  $UAS$   
627 and  $f$  distributions were thus obtained compared to those of the monodispersed raw biomass. However, the  
628 computing time was greatly increased due to the presence of finer particles which led to a higher number of  
629 particles to be simulated to reach the same fill ratio (19 376 for the polydispersed system compared to 13 122  
630 for the monodisperse raw biomass). This suggests that a polydisperse system could be adequately  
631 represented by a simplified monodisperse population, thus saving time in terms of calculation. Further work  
632 with a higher degree of polydispersity might be required to reinforce these findings.

633  
634  
635  
636  
637

638 *Figure 12. Comparison of DEM results between monodisperse raw biomass (100% volume fraction at  $d = 746 \mu m$ ) and a polydisperse*  
639 *sample (three particle sizes:  $d = 500, 746$  and  $890 \mu m$  at 25, 50 and 25% volume fractions, respectively). (a) Evolution of the  $\alpha$  angle*  
640 *over time (for clarity, the y-axis of the data sets is not the same; e.g. the raw biomass results should be read on the left y-axis). (b) UAS*  
641 *cumulative distributions. (c)  $f$  cumulative distributions.*

642

## 643 6. CONCLUSIONS

644 Rotating drum tests are pertinent for studying bulk flow of granular materials in a non-consolidated and  
645 dynamic conditioning. In this study, we evaluated the ability of DEM simulations for assessing flow behavior  
646 of raw and torrefied milled biomass in a rotating drum.

647 The challenging characteristics of biomass particles with respect to simulations (submillimetric size,  
648 elongated shape, cohesive nature) were integrated in a DEM model using a coarse-grained multisphere  
649 approach for shape representation, along with a cohesive SJKR contact model. Bulk measurements of the  
650 angle-of-repose, the bulk density and a retainment ratio were used for calibration of the interparticle  
651 coefficients of sliding friction, rolling friction and the Cohesion Energy Density.

652 Qualitative comparison with the experimental behavior in a rotating drum system made it possible to  
653 reduce the number of optimal sets of calibrated DEM parameters. To reproduce the experimental cohesive  
654 behavior, it was therefore necessary to select a set of optimum interparticle parameters among those with  
655 the highest cohesive energy density values. For raw biomass the optimal value of  $CED$  was ca.  $50 \text{ kJ/m}^3$   
656 while for torrefied powders  $CED$  values were higher and closer to the upper limit of tested values  
657 ( $80 \text{ kJ/m}^3$ ).

658 The selected parameters led to a realistic representation of the avalanche motion for the biomass  
659 materials that could be achieved through the combined effects of an elongated particle shape and  
660 interparticle cohesion. The calibrated DEM parameters obtained from relatively easy-to-implement bulk  
661 setups can therefore be used to reliably reproduce a dynamic non-consolidated flow of biomass particles,  
662 the latter being much more expensive to use as calibration setup in terms of computing time as stated in  
663 previous research.

664 Overall, the granular flow dynamics was correctly captured by the DEM simulations. A continuous  
665 regime of flow developed for non-cohesive glass beads, while avalanches of particle clusters with centroid  
666 angle variations of up to  $20^\circ$  were characteristic of biomass powders. Discrepancy between DEM results  
667 and the experimental values of the Upper Angle of stability remained under 7 % and qualitatively similar  
668 distributions between experiments and simulations were obtained for the fraction of revolution to trigger  
669 events and size of avalanches. Although significant differences were found regarding the irregularity of the

670 free-surface profile, similar numerical and experimental rankings of flowability could be established. This  
671 confirms the suitability of the DEM simulations for assessing flow of cohesive biomass particles in a free-  
672 surface dynamic system.

673 DEM simulations were useful to study the isolated effects of particle shape and cohesion on the flow  
674 behavior. An increase of 18 % in the average centroid angle was observed when elongated particles were  
675 compared to spherical particles of the same equivalent size. This increase rises to ca. +36 % when a cohesive  
676 interaction (50 kJ/m<sup>3</sup>) between particles is added.

677 While physical sound results were obtained using parameters calibrated using simple-to-implement bulk  
678 setups, the robustness of these parameters remains to be further clarified through, for example, the  
679 investigation of other flow conditions (including under consolidation). Future studies could also explore the  
680 effects of the particle-wall interaction parameters, polydispersity as well as more elaborate particle shape  
681 representations that are more favorable to particle interlocking.

682

## 683 Acknowledgments

684 The authors would like to gratefully acknowledge the support of the French Ministry of Higher  
685 Education and Research as well as the French-Dutch Network (Eole Scholarship) for their financial support.  
686 We are especially thankful to the French Council for Poplar (CNP) and the Huberlant sawmill (Cormicy,  
687 France) for kindly providing the raw wood used in this work.

688

## 689 References

- 690 [1] J. Dai, H. Cui, J.R. Grace, Biomass feeding for thermochemical reactors, *Prog. Energy Combust.*  
691 *Sci.* 38 (2012) 716–736. doi:10.1016/j.pecs.2012.04.002.
- 692 [2] Z. Guo, X. Chen, H. Liu, Q. Guo, X. Guo, H. Lu, Theoretical and experimental investigation on  
693 angle of repose of biomass-coal blends, *Fuel*. 116 (2014) 131–139. doi:10.1016/j.fuel.2013.07.098.
- 694 [3] M. Asadullah, Barriers of commercial power generation using biomass gasification gas: A review,  
695 *Renew. Sustain. Energy Rev.* 29 (2014) 201–215. doi:10.1016/j.rser.2013.08.074.
- 696 [4] J.S. Tumuluru, S. Sokhansanj, J.R. Hess, C.T. Wright, R.D. Boardman, A review on biomass  
697 torrefaction process and product properties for energy applications, *Ind. Biotechnol.* 7 (2011) 384–  
698 401. doi:10.1089/ind.2011.0014.
- 699 [5] W.H. Chen, J. Peng, X.T. Bi, A state-of-the-art review of biomass torrefaction, densification and  
700 applications, *Renew. Sustain. Energy Rev.* 44 (2015) 847–866. doi:10.1016/j.rser.2014.12.039.
- 701 [6] J. Pachón-Morales, J. Colin, F. Pierre, F. Puel, P. Perré, Effect of torrefaction intensity on the flow  
702 properties of lignocellulosic biomass powders, *Biomass and Bioenergy*. 120 301–312.  
703 doi:10.1016/j.biombioe.2018.11.017.
- 704 [7] G. Xu, M. Li, P. Lu, Experimental investigation on flow properties of different biomass and torrefied  
705 biomass powders, *Biomass and Bioenergy*. 122 (2019) 63–75. doi:10.1016/j.biombioe.2019.01.016.
- 706 [8] M.R. Wu, D.L. Schott, G. Lodewijks, Physical properties of solid biomass, *Biomass and Bioenergy*.  
707 35 (2011) 2093–2105. doi:10.1016/j.biombioe.2011.02.020.
- 708 [9] F. Miccio, D. Barletta, M. Poletto, Flow properties and arching behavior of biomass particulate

- 709 solids, *Powder Technol.* 235 (2013) 312–321. doi:10.1016/j.powtec.2012.10.047.
- 710 [10] F. Miccio, N. Silvestri, D. Barletta, M. Poletto, Characterization of woody biomass flowability,  
711 *Chem. Eng. Trans.* 24 (2011) 643–648. doi:10.3303/CET1124108.
- 712 [11] D. Barletta, R.J. Berry, S.H. Larsson, T.A. Lestander, M. Poletto, Á. Ramírez-Gómez, Assessment  
713 on bulk solids best practice techniques for flow characterization and storage/handling equipment  
714 design for biomass materials of different classes, *Fuel Process. Technol.* 138 (2015) 540–554.  
715 doi:10.1016/j.fuproc.2015.06.034.
- 716 [12] J. Falk, R.J. Berry, M. Broström, S.H. Larsson, Mass flow and variability in screw feeding of biomass  
717 powders — Relations to particle and bulk properties, *Powder Technol.* 276 (2015) 80–88.  
718 doi:10.1016/j.powtec.2015.02.023.
- 719 [13] M. Zulfiqar, B. Moghtaderi, T.F. Wall, Flow properties of biomass and coal blends, *Fuel Process.*  
720 *Technol.* 87 (2006) 281–288. doi:10.1016/j.fuproc.2004.10.007.
- 721 [14] R.G. Iacocca, R.M. German, The experimental evaluation of die compaction lubricants using  
722 deterministic chaos theory, *Powder Technol.* 102 (1999) 253–265. doi:10.1016/S0032-  
723 5910(98)00217-4.
- 724 [15] Y.L. Xiao, E. Specht, J. Mellmann, Experimental study of the lower and upper angles of repose of  
725 granular materials in rotating drums, *Powder Technol.* 154 (2005) 125–131.  
726 doi:10.1016/j.powtec.2005.04.040.
- 727 [16] J. Mellmann, The transverse motion of solids in rotating cylinders-forms of motion and transition  
728 behavior, *Powder Technol.* 118 (2001) 251–270. doi:10.1016/S0032-5910(00)00402-2.
- 729 [17] R. Li, H. Yang, G. Zheng, Q.C. Sun, Granular avalanches in slumping regime in a 2D rotating drum,  
730 *Powder Technol.* 326 (2018) 322–326. doi:10.1016/j.powtec.2017.12.032.
- 731 [18] H. Yang, G.L. Jiang, H.Y. Saw, C. Davies, M.J. Biggs, V. Zivkovic, Granular dynamics of cohesive  
732 powders in a rotating drum as revealed by speckle visibility spectroscopy and synchronous  
733 measurement of forces due to avalanching, *Chem. Eng. Sci.* 146 (2016) 1–9.  
734 doi:10.1016/j.ces.2016.02.023.
- 735 [19] V.R. Nalluri, M. Kuentz, Flowability characterisation of drug-excipient blends using a novel powder  
736 avalanching method, *Eur. J. Pharm. Biopharm.* 74 (2010) 388–396. doi:10.1016/j.ejpb.2009.09.010.
- 737 [20] A.W. Alexander, B. Chaudhuri, A. Faqih, F.J. Muzzio, C. Davies, M.S. Tomassone, Avalanching  
738 flow of cohesive powders, *Powder Technol.* 164 (2006) 13–21. doi:10.1016/j.powtec.2006.01.017.
- 739 [21] M.A.S. Quintanilla, J.M. Valverde, A. Castellanos, The transitional behaviour of avalanches in  
740 cohesive granular materials, *J. Stat. Mech. Theory Exp.* (2006). doi:10.1088/1742-  
741 5468/2006/07/P07015.
- 742 [22] S.C. Thakur, J.Y. Ooi, M.B. Wojtkowski, O.I. Imole, V. Magnanimo, H. Ahmadian, E.C. Montes,  
743 M. Ramaioli, Characterisation of cohesive powders for bulk handling and dem modelling, 3rd Int.  
744 *Conf. Part. Methods Fundam. Appl. Part.* 2013. (2013) 310–321. doi:10.1063/1.4812098.
- 745 [23] V. Jaggi, M.C. Leaper, A. Ingham, Measuring the flow properties of small powder samples using an  
746 avalanche tester, *Dry. Technol.* 34 (2016) 723–728. doi:10.1080/07373937.2015.1072093.
- 747 [24] E. Emery, J. Oliver, T. Pugsley, J. Sharma, J. Zhou, Flowability of moist pharmaceutical powders,  
748 *Powder Technol.* 189 (2009) 409–415. doi:10.1016/j.powtec.2008.06.017.

- 749 [25] M. Wojtkowski, O.I. Imole, M. Ramaioli, E. Chaóvez Montes, S. Luding, Behavior of cohesive  
750 powder in rotating drums, *AIP Conf. Proc.* 1542 (2013) 983–986. doi:10.1063/1.4812098.
- 751 [26] P.A. Cundall, O.D.L. Strack, A discrete numerical model for granular assemblies, *Géotechnique*. 29  
752 (1979) 47–65. doi:10.1680/geot.1979.29.1.47.
- 753 [27] Z. Hu, X. Liu, W. Wu, Study of the critical angles of granular material in rotary drums aimed for fast  
754 DEM model calibration, *Powder Technol.* 340 (2018) 563–569. doi:10.1016/j.powtec.2018.09.065.
- 755 [28] R.Y. Yang, R.P. Zou, A.B. Yu, Microdynamic analysis of particle flow in a horizontal rotating drum,  
756 *Powder Technol.* 130 (2003) 138–146. doi:10.1016/S0032-5910(02)00257-7.
- 757 [29] E. Alizadeh, F. Bertrand, J. Chaouki, Comparison of DEM Results and Lagrangian Experimental  
758 Data for the Flow and Mixing of Granules in a Rotating Drum, *AIChE J.* 60 (2014) 60–75.  
759 doi:10.1002/aic.14259.
- 760 [30] R.Y. Yang, A.B. Yu, L. McElroy, J. Bao, Numerical simulation of particle dynamics in different flow  
761 regimes in a rotating drum, *Powder Technol.* 188 (2008) 170–177.  
762 doi:10.1016/j.powtec.2008.04.081.
- 763 [31] H. Chen, Y.G. Xiao, Y.L. Liu, Y.S. Shi, Effect of Young’s modulus on DEM results regarding  
764 transverse mixing of particles within a rotating drum, *Powder Technol.* (2017).  
765 doi:10.1016/j.powtec.2017.05.047.
- 766 [32] D.A. Santos, M.A.S. Barrozo, C.R. Duarte, F. Weigler, J. Mellmann, Investigation of particle  
767 dynamics in a rotary drum by means of experiments and numerical simulations using DEM, *Adv.*  
768 *Powder Technol.* 27 (2016) 692–703. doi:10.1016/j.appt.2016.02.027.
- 769 [33] C.M. Dury, G.H. Ristow, J.L. Moss, M. Nakagawa, Boundary effects on the angle of repose in  
770 rotating cylinders, *Phys. Rev. E - Stat. Physics, Plasmas, Fluids, Relat. Interdiscip. Top.* 57 (1998)  
771 4491–4497. doi:10.1103/PhysRevE.57.4491.
- 772 [34] H.R. Norouzi, R. Zarghami, N. Mostoufi, Insights into the granular flow in rotating drums, *Chem.*  
773 *Eng. Res. Des.* 102 (2015) 12–25. doi:10.1016/j.cherd.2015.06.010.
- 774 [35] R.N. Cunha, K.G. Santos, R.N. Lima, C.R. Duarte, M.A.S. Barrozo, Repose angle of monoparticles  
775 and binary mixture: An experimental and simulation study, *Powder Technol.* 303 (2016) 203–211.  
776 doi:10.1016/j.powtec.2016.09.023.
- 777 [36] S.R. Mead, P.W. Cleary, G.K. Robinson, Characterising the failure and repose angles of irregularly  
778 shaped three-dimensional particles using DEM, *Ninth Int. Conf. CFD Miner. Process Ind. CSIRO,*  
779 *Melbourne, Aust.* (2012) 1–6.
- 780 [37] G.G. Pereira, S. Pucilowski, K. Liffman, P.W. Cleary, Streak patterns in binary granular media in a  
781 rotating drum, *Appl. Math. Model.* 35 (2011) 1638–1646. doi:10.1016/j.apm.2010.09.040.
- 782 [38] S.T. Nase, W.L. Vargas, A.A. Abatan, J.J. McCarthy, Discrete characterization tools for cohesive  
783 granular material, *Powder Technol.* 116 (2001) 214–223. doi:10.1016/S0032-5910(00)00398-3.
- 784 [39] D. Höhner, S. Wirtz, V. Scherer, A study on the influence of particle shape and shape approximation  
785 on particle mechanics in a rotating drum using the discrete element method, *Powder Technol.* 253  
786 (2014) 256–265. doi:10.1016/j.powtec.2013.11.023.
- 787 [40] C.J. Coetzee, Particle upscaling: Calibration and validation of the discrete element method, *Powder*  
788 *Technol.* 344 (2019) 487–503. doi:10.1016/J.POWTEC.2018.12.022.

- 789 [41] Y.T. Feng, D.R.J. Owen, Discrete element modelling of large scale particle systems—I: exact scaling  
790 laws, *Comput. Part. Mech.* 1 (2014) 159–168. doi:10.1007/s40571-014-0010-y.
- 791 [42] A. Wachs, L. Girolami, G. Vinay, G. Ferrer, Grains3D, a flexible DEM approach for particles of  
792 arbitrary convex shape - Part I: Numerical model and validations, *Powder Technol.* 224 (2012) 374–  
793 389. doi:10.1016/j.powtec.2012.03.023.
- 794 [43] M.W. Johnstone, Calibration of DEM models for granular materials using bulk physical tests, (2010).  
795 <http://hdl.handle.net/1842/4655>.
- 796 [44] M. Marigo, Discrete element method modelling of complex granular motion in mixing vessels:  
797 evaluation and validation, (2012) 1–341. <http://core.kmi.open.ac.uk/download/pdf/8821055.pdf>.
- 798 [45] M. Kodam, R. Bharadwaj, J. Curtis, B. Hancock, C. Wassgren, Cylindrical object contact detection  
799 for use in discrete element method simulations. Part I – Contact detection algorithms, (2010).  
800 doi:10.1016/j.ces.2010.08.006.
- 801 [46] B.K. Mishra, C. Thornton, D. Bhimji, A preliminary numerical investigation of agglomeration in a  
802 rotary drum, *Miner. Eng.* 15 (2002) 27–33. doi:10.1016/S0892-6875(01)00194-7.
- 803 [47] R. Brewster, G.S. Grest, A.J. Levine, Effects of cohesion on the surface angle and velocity profiles  
804 of granular material in a rotating drum, *Phys. Rev. E - Stat. Nonlinear, Soft Matter Phys.* 79 (2009)  
805 1–7. doi:10.1103/PhysRevE.79.011305.
- 806 [48] M. Sebastian Escotet-Espinoza, C.J. Foster, M. Ierapetritou, Discrete Element Modeling (DEM) for  
807 mixing of cohesive solids in rotating cylinders, *Powder Technol.* 335 (2018) 124–136.  
808 doi:10.1016/j.powtec.2018.05.024.
- 809 [49] A.M. Faqih, B. Chaudhuri, A.W. Alexander, C. Davies, F.J. Muzzio, M. Silvina Tomassone, An  
810 experimental/computational approach for examining unconfined cohesive powder flow, *Int. J.*  
811 *Pharm.* 324 (2006) 116–127. doi:10.1016/j.ijpharm.2006.05.067.
- 812 [50] S. Just, G. Toschkoff, A. Funke, D. Djuric, G. Scharrer, J. Khinast, K. Knop, P. Kleinebudde,  
813 Experimental Analysis of Tablet Properties for Discrete Element Modeling of an Active Coating  
814 Process, *AAPS PharmSciTech.* 14 (2013) 402–411. doi:10.1208/s12249-013-9925-5.
- 815 [51] M. Combarros, H.J. Feise, H. Zetzener, A. Kwade, Segregation of particulate solids: Experiments  
816 and DEM simulations, *Particuology.* 12 (2014) 25–32. doi:10.1016/j.partic.2013.04.005.
- 817 [52] M. Marigo, E.H. Stitt, Discrete element method (DEM) for industrial applications: Comments on  
818 calibration and validation for the modelling of cylindrical pellets, *KONA Powder Part. J.* 32 (2015)  
819 236–252. doi:10.14356/kona.2015016.
- 820 [53] T. Pöschel, C. Saluena, T. Schwager, Can we scale granular systems?, (2001).
- 821 [54] M. Sakai, S. Koshizuka, Large-scale discrete element modeling in pneumatic conveying, *Chem. Eng.*  
822 *Sci.* 64 (2009) 533–539. doi:10.1016/j.ces.2008.10.003.
- 823 [55] D.S. Nasato, C. Goniva, S. Pirker, C. Kloss, Coarse graining for large-scale DEM simulations of  
824 particle flow - An investigation on contact and cohesion models, *Procedia Eng.* 102 (2015) 1484–  
825 1490. doi:10.1016/j.proeng.2015.01.282.
- 826 [56] P.W. Cleary, M.L. Sawley, DEM modelling of industrial granular flows: 3D case studies and the  
827 effect of particle shape on hopper discharge, *Appl. Math. Model.* 26 (2002) 89–111.  
828 doi:10.1016/S0307-904X(01)00050-6.

- 829 [57] T. Roessler, A. Katterfeld, Scaling of the angle of repose test and its influence on the calibration of  
830 DEM parameters using upscaled particles, *Powder Technol.* 330 (2018) 58–66.  
831 doi:10.1016/j.powtec.2018.01.044.
- 832 [58] S. Luding, M.M. Msm, Mesoscale modeling of particles and particles in fluids - Multi-Scale ( Models  
833 ) and - Continuum Theory ( Applications ) - Jamming and un-jamming, (2013).
- 834 [59] J. Pachón-Morales, H. Do, J. Colin, F. Puel, P. Perré, D. Schott, DEM modelling for flow of cohesive  
835 lignocellulosic biomass powders: Model calibration using bulk tests, *Adv. Powder Technol.* (2019).  
836 doi:10.1016/j.appt.2019.01.003.
- 837 [60] J. Colin, Séchage en continu du bois énergie comme moyen de conditionnement en vue de sa  
838 conservation thermochimique: approches expérimentale et numérique, *AgroParisTech*, 2011.  
839 <https://pastel.archives-ouvertes.fr/pastel-00861231>.
- 840 [61] G. Almeida, D.V.B. Santos, P. Perré, Mild pyrolysis of fast-growing wood species (Caribbean pine  
841 and Rose gum): Dimensional changes predicted by the global mass loss, *Biomass and Bioenergy.* 70  
842 (2014) 407–415. doi:10.1016/j.biombioe.2014.07.028.
- 843 [62] F. Pierre, G. Almeida, F. Huber, P. Jacquin, P. Perré, An original impact device for biomass  
844 characterisation: Results obtained for spruce and poplar at different moisture contents, *Wood Sci.*  
845 *Technol.* 47 (2013) 537–555. doi:10.1007/s00226-012-0512-9.
- 846 [63] J. Pachón-Morales, J. Colin, F. Pierre, T. Champavert, F. Puel, P. Perré, Flowability of lignocellulosic  
847 biomass powders: Influence of torrefaction intensity, *EPJ Web Conf.* 140 (2017).  
848 doi:10.1051/epjconf/201714013017.
- 849 [64] T. Lichtenegger, S. Pirker, CFD-DEM modeling of strongly polydisperse particulate systems,  
850 *Powder Technol.* 325 (2018) 698–711. doi:10.1016/j.powtec.2017.11.058.
- 851 [65] Sympatec, QICPIC GmbH, (2018). [https://www.sympatec.com/en/particle-](https://www.sympatec.com/en/particle-measurement/sensors/dynamic-image-analysis/qicpic/)  
852 [measurement/sensors/dynamic-image-analysis/qicpic/](https://www.sympatec.com/en/particle-measurement/sensors/dynamic-image-analysis/qicpic/) (accessed July 11, 2018).
- 853 [66] J. Pachón-Morales, Torrefaction and grinding of lignocellulosic biomass for its thermochemical  
854 valorization: influence of pretreatment conditions on powder flow properties, *Université Paris-*  
855 *Saclay*, 2019. <http://www.theses.fr/2019SACL051>.
- 856 [67] P. Tegzes, T. Vicsek, P. Schiffer, Development of correlations in the dynamics of wet granular  
857 avalanches, *Phys. Rev. E - Stat. Physics, Plasmas, Fluids, Relat. Interdiscip. Top.* 67 (2003) 17.  
858 doi:10.1103/PhysRevE.67.051303.
- 859 [68] C. Kloss, C. Goniva, A. Hager, S. Amberger, S. Pirker, Models, algorithms and validation for  
860 opensource DEM and CFD-DEM, *Prog. Comput. Fluid Dyn. An Int. J.* 12 (2012) 140.  
861 doi:10.1504/PCFD.2012.047457.
- 862 [69] Q.J. Zheng, H.P. Zhu, A.B. Yu, Finite element analysis of the rolling friction of a viscous particle  
863 on a rigid plane, *Powder Technol.* 207 (2011) 401–406. doi:10.1016/j.powtec.2010.11.026.
- 864 [70] M. Obermayr, C. Vrettos, P. Eberhard, T. Däuwel, A discrete element model and its experimental  
865 validation for the prediction of draft forces in cohesive soil, *J. Terramechanics.* 53 (2014) 93–104.  
866 doi:10.1016/j.jterra.2014.04.003.
- 867 [71] K. Iwashita, M. Oda, Rolling Resistance at Contacts in Simulation of Shear Band Development by  
868 DEM, *J. Eng. Mech.* 124 (1998) 285–292. doi:10.1061/(ASCE)0733-9399(1998)124:3(285).

- 869 [72] K.L. Johnson, K. Kendall, A.D. Roberts, Surface Energy and the Contact of Elastic Solids, *Proc. R. Soc. A Math. Phys. Eng. Sci.* 324 (1971) 301–313. doi:10.1098/rspa.1971.0141.  
870
- 871 [73] Z. Shen, M. Jiang, C. Thornton, DEM simulation of bonded granular material. Part I: Contact model  
872 and application to cemented sand, *Comput. Geotech.* 75 (2016) 192–209.  
873 doi:10.1016/j.compgeo.2016.02.007.
- 874 [74] S.C. Thakur, J.P. Morrissey, J. Sun, J.F. Chen, J.Y. Ooi, Micromechanical analysis of cohesive  
875 granular materials using the discrete element method with an adhesive elasto-plastic contact model,  
876 *Granul. Matter.* 16 (2014) 383–400. doi:10.1007/s10035-014-0506-4.
- 877 [75] GmbH DCS Computing, gran cohesion sjkr model — LIGGGHTS v3.X documentation, (n.d.).  
878 [https://www.cfdem.com/media/DEM/docu/gran\\_cohesion\\_sjkr.html](https://www.cfdem.com/media/DEM/docu/gran_cohesion_sjkr.html) (accessed September 7,  
879 2018).
- 880 [76] J.F. Favier, M.H. Abbaspour-Fard, M. Kremmer, Modeling nonspherical particles using  
881 multispheres, *J. Eng. Mech.* 127 (2001) 971–977.
- 882 [77] H. Kruggel-Emden, S. Rickelt, S. Wirtz, V. Scherer, A study on the validity of the multi-sphere  
883 Discrete Element Method, *Powder Technol.* 188 (2008) 153–165.  
884 doi:10.1016/j.powtec.2008.04.037.
- 885 [78] R. Maione, S. Kiesgen De Richter, G. Mauviel, G. Wild, DEM investigation of granular flow and  
886 binary mixture segregation in a rotating tumbler: Influence of particle shape and internal baffles,  
887 *Powder Technol.* 286 (2015) 732–739. doi:10.1016/j.powtec.2015.09.011.
- 888 [79] D. Markauskas, Á. Ramírez-Gómez, R. Kačianauskas, E. Zdancevičius, Maize grain shape  
889 approaches for DEM modelling, *Comput. Electron. Agric.* 118 (2015) 247–258.  
890 doi:10.1016/j.compag.2015.09.004.
- 891 [80] D. Markauskas, R. Kačianauskas, Investigation of rice grain flow by multi-sphere particle model with  
892 rolling resistance, *Granul. Matter.* 13 (2011) 143–148. doi:10.1007/s10035-010-0196-5.
- 893 [81] M. Rackl, F. Top, C.P. Molhoek, D.L. Schott, Biomass and Bioenergy Feeding system for wood  
894 chips : A DEM study to improve equipment performance, *Biomass and Bioenergy.* 98 (2017) 43–  
895 52. doi:10.1016/j.biombioe.2017.01.003.
- 896 [82] H.Q. Do, A.M. Aragón, D.L. Schott, A calibration framework for discrete element model parameters  
897 using genetic algorithms, *Adv. Powder Technol.* (2018) 1–11. doi:10.1016/j.apt.2018.03.001.
- 898 [83] K. Deb, A. Pratap, S. Agarwal, T. Meyarivan, A fast and elitist multiobjective genetic algorithm:  
899 NSGA-II, *IEEE Trans. Evol. Comput.* 6 (2002) 182–197. doi:10.1109/4235.996017.
- 900 [84] J. Härtl, J.Y. Ooi, Numerical investigation of particle shape and particle friction on limiting bulk  
901 friction in direct shear tests and comparison with experiments, *Powder Technol.* 212 (2011) 231–  
902 239. doi:10.1016/j.powtec.2011.05.022.
- 903 [85] Á. Ramírez-Gómez, E. Gallego, J.M. Fuentes, C. González-Montellano, F. Ayuga, Values for  
904 particle-scale properties of biomass briquettes made from agroforestry residues, *Particuology.* 12  
905 (2014) 100–106. doi:10.1016/j.partic.2013.05.007.
- 906 [86] D. Mateo-Ortiz, R. Méndez, Microdynamic analysis of particle flow in a confined space using DEM:  
907 The feed frame case, *Adv. Powder Technol.* 27 (2016) 1597–1606. doi:10.1016/j.apt.2016.05.023.
- 908 [87] M. Florian-Algarin, R. Mendez, Blend Uniformity and Powder Phenomena Inside the Continuous

- 909 Tumble Mixer Using DEM Simulations, *AIChE J.* 61 (2015) 792–801. doi:10.1002/aic.14694.
- 910 [88] Y.T. Feng, K. Han, D.R.J. Owen, J. Loughran, On upscaling of discrete element models: Similarity  
911 principles, *Eng. Comput.* (Swansea, Wales). 26 (2009) 599–609. doi:10.1108/02644400910975405.
- 912 [89] W. Yang, Z. Zhou, D. Pinson, A. Yu, Periodic boundary conditions for discrete element method  
913 simulation of particle flow in cylindrical vessels, *Ind. Eng. Chem. Res.* 53 (2014) 8245–8256.  
914 doi:10.1021/ie404158e.
- 915 [90] X. Liu, Z. Hu, W. Wu, J. Zhan, F. Herz, E. Specht, DEM study on the surface mixing and whole  
916 mixing of granular materials in rotary drums, *Powder Technol.* 315 (2017) 438–444.  
917 doi:10.1016/j.powtec.2017.04.036.
- 918 [91] J. Pachón-Morales, J. Colin, J. Casalinho, P. Perré, F. Puel, Flowability characterization of torrefied  
919 biomass powders : static and dynamic testing Keywords :, *Submitt. to Biomass Bioenergy.* (2019) 1–  
920 31.
- 921